

## Cosmogenic Radionuclide Records of Hayabusa Aggregate and Particle Samples

Kunihiko Nishiizumi<sup>1</sup>, Marc W. Caffee<sup>2</sup>, Keisuke Nagao<sup>3</sup>, Kees C. Welten<sup>1</sup>, Jozef Masarik<sup>4</sup>

<sup>1</sup>Space Sciences Laboratory, Univ. of California, Berkeley, CA 94720-7450, USA., <sup>2</sup>Dept. of Physics & Astronomy, Purdue Univ., West Lafayette, IN 47907-2036, USA., <sup>3</sup>Div. of Polar Earth-System Sci., KOPRI, Incheon 21990, Korea, <sup>4</sup>Faculty of Math. & Physics, Comenius Univ., SK-842 15, Bratislava, Slovakia

Hayabusa2 arrived at the C-type asteroid 162173 Ryugu in June 2018, and successfully collected surface samples from two sampling sites, returning ~5.4 g of material to Earth on December 6, 2020. The surface samples stored in Chamber A were collected by the 1<sup>st</sup> touchdown (TD) on Ryugu's surface on February 21, 2019. A crater (diameter of ~14 m) on Ryugu's surface was made using a collision device - denoted "Small Carry-on Impactor (SCI)" - on April 5, 2019 [1]. The samples in Chamber C were collected proximal to the north side of this artificial crater by the 2<sup>nd</sup> TD on July 11, 2019 and possibly contain ejecta from the crater [2]. Distance between TD1 and TD2 is ~820 m.

Our studies are based on the measurement of those nuclides produced in asteroidal surface materials by cosmic rays - both solar (SCR) and galactic cosmic rays (GCR). Cosmic-ray-produced (cosmogenic) nuclides are used to determine the duration and nature of the exposure of materials to energetic particles. Our goals are to understand both the fundamental processes on the asteroidal surface and the evolutionary history of its surface materials. For Hayabusa2 samples, there are several specific questions we aim to address: (1) are the Chamber C samples, collected during the 2<sup>nd</sup> TD ejecta deposits from the artificial crater, (2) if so, what is the original depth of each recovered sample in the Ryugu regolith, and (3) what is the surface exposure time, mixing rate, and erosion/escape rate of Ryugu's surface? To answer these questions, we were allocated and received particles from Chamber A and Chamber C for measurements of cosmogenic radionuclides and noble gases as a part of initial analysis of Ryugu. We have measured cosmogenic <sup>10</sup>Be ( $t_{1/2} = 1.36 \times 10^6$  yr), <sup>26</sup>Al ( $7.05 \times 10^5$  yr), <sup>36</sup>Cl ( $3.01 \times 10^5$  yr), and stable noble gases in those samples [3-5]. Based on noble gas analysis of ~2 dozen Ryugu samples, we found that cosmic ray exposure (CRE) ages of Chamber A (surface) samples, A0105, range from 2.9 to 7.5 Myr and Chamber C (sub-surface) samples, C0106, range from 1.6 to 5.8 Myr based on <sup>21</sup>Ne concentrations [3, 6]. We also found that four C0106 particles were exposed at depth of ~50, 110, 130, and 145 g/cm<sup>2</sup> respectively and had different CRE ages based on cosmogenic nuclide measurements [3, 5].

To further study of the exposure condition of Ryugu surface materials, we obtained one grain, A0130, from Chamber A and 3 grains, C0012, 0162, and 0182 from Chamber C. In addition, we obtained two aggregate samples, A0221 and C0212, in order to determine average exposure ages and depths for both Chamber A and C samples. As shown above, each grain had different exposure histories (age and depth). This is similar to what we found for exposure histories of individual grains of lunar core samples. While cosmogenic radionuclides of lunar bulk soils show smooth depth profiles, the measured radionuclide concentrations of individual rock fragments at the same depth show deviations from the smooth depth profiles [7].

Each sample was gently crushed by a mortar and pestle made from sapphire and then divided into two fractions, one fraction for cosmogenic radionuclides (this work) and one for noble gases measurements [8]. The samples were individually transferred to a small Al weighing boat and the masses were determined using an ultra-micro balance. For cosmogenic radionuclide analysis, the sample was transferred to a Teflon bomb and dissolved with HF and HNO<sub>3</sub> mixture in the presence of Be and Cl carriers. After Cl was separated as AgCl for <sup>36</sup>Cl measurements, a small analysis aliquot was taken for chemical analysis by ICP-OES. Beryllium, Al, and Mn were separated by ion chromatography, using anion and cation ion exchange columns, and Be and Al were purified for AMS measurements. To serve as a baseline comparison, a few grains of the Orgueil CI chondrite were analyzed using the same protocols. Beryllium-10 and <sup>26</sup>Al AMS analyses were performed at PRIME Lab, Purdue University [9]. Measured isotopic ratios were normalized by AMS standards [10, 11] and converted to radionuclide concentrations (dpm/kg).

Chemical compositions in Ryugu samples measured by ICP-OES are shown in Table 1. Since sample sizes are slightly larger than previous Ryugu initial analysis, data show less scatter. Bulk chemical compositions of samples from TD1 and TD2 determined using ICP-MS [12] are also shown in the table. Our analysis of A0221 and C0212 are in good agreement with analysis of TD1 and TD2 samples determined by [12]. Noticeably, both our two samples and published analysis of TD1 and TD2 samples [12] were obtained from aggregate samples and not individual grains. Although [12] concluded that there are no systematic differences in chemical composition between the samples from TD1 and TD2 sites, our limited measurements indicate that Ca is slightly higher and Fe is lower in TD1 samples than that of TD2.

Table 1. Chemical compositions in Ryugu samples and Orgueil CI chondrite.

Sample	Mg (%)	Al (%)	K (ppm)	Ca (%)	Ti (ppm)	Mn (ppm)	Fe (%)	Co (ppm)	Ni (%)
A0130	9.32	0.94	720	1.45	520	1990	18.39	540	1.13
A0221	10.84	0.90	520	1.69	530	3040	19.76	560	1.20
C0012	10.54	0.91	600	1.09	460	2020	21.15	600	1.31
C0012	10.74	0.91	580	1.18	490	2340	20.11	560	1.21
C0162	10.81	0.90	570	1.08	570	2120	20.75	560	1.26
C0182	9.36	0.84	400	0.95	510	1510	18.63	520	1.13
C0212	10.77	0.98	550	1.18	510	2370	20.53	590	1.26
Ryugu (TD1)*	10.69	0.86	520	1.63	480	3000	19.49	550	1.18
Ryugu (TD2)*	10.42	0.90	600	1.37	470	2490	20.22	590	1.22
Orgueil CI	7.37	0.64	440	0.60	340	1380	14.23	400	1.18
Orgueil CI <sup>#</sup>	9.63	0.60	530	0.76	-	1680	17.76	540	1.04

\*[12], <sup>#</sup>Previous measurement (unpublished 2003)

Cosmogenic nuclide <sup>10</sup>Be and <sup>26</sup>Al concentrations in Ryugu samples are shown in Table 2 along with that of Orgueil CI chondrite. Using the MCNP Code System [13], we calculated the GCR production rates of <sup>10</sup>Be and <sup>26</sup>Al by spallation reactions for a body having a 2 $\pi$  geometry with Ryugu's chemical composition [12]. Based on the comparison of the observed radionuclide concentrations with model calculated <sup>10</sup>Be and <sup>26</sup>Al production rate depth profiles, assuming the radionuclide concentrations in Ryugu are saturated, we obtained the first order estimation of exposure depth of each sample and shown in Table 2. Based on those depths we calculated <sup>21</sup>Ne production rates and calculated <sup>21</sup>Ne CRE ages in each sample [8]. The calculated exposure depths and CRE ages of each grain obtained by TD2 scatter, in similar fashion as previous works [3, 5]. The preliminary estimation of average exposure depth of aggregate sample A0221 is somewhat deeper than those of each grain obtained from TD1. The depth range of aggregate sample C0212 collected by TD2 is estimated to be 110 - 140 g/cm<sup>2</sup> based on <sup>10</sup>Be concentration. The <sup>26</sup>Al concentration of C0212 indicates much shallow depth of 10 - 90 g/cm<sup>2</sup>. One possible explanation is that C0212 contains a small amount of surface material that contains high SCR produced <sup>26</sup>Al. The measurement of thermal neutron-capture produced <sup>41</sup>Ca ( $t_{1/2} = 1.0 \times 10^5$  yr) - in progress - is critical to further constrain the exposure depth of each sample.

Table 2. Cosmogenic nuclide <sup>10</sup>Be and <sup>26</sup>Al concentrations in Ryugu samples and Orgueil CI chondrite.

Sample	Mass (mg)	<sup>10</sup> Be (dpm/kg)	<sup>26</sup> Al (dpm/kg)	Depth (g/cm <sup>2</sup> )
A0130	0.676	9.94 ± 0.29	29.2 ± 1.3	10 - 70
A0221	10.718	11.23 ± 0.10	27.4 ± 0.6	70 - 100
C0012	4.200	7.50 ± 0.10	24.3 ± 0.8	90 - 140
C0012	7.274	7.43 ± 0.15	23.3 ± 0.8	110 - 150
C0162	1.531	7.58 ± 0.21	24.6 ± 1.0	95 - 145
C0182	0.983	6.28 ± 0.15	25.3 ± 1.3	85 - 135
C0212	8.406	9.06 ± 0.09	29.3 ± 0.6	110 -140
Orgueil CI	6.000	14.91 ± 0.31	35.9 ± 1.2	-
Orgueil CI <sup>#</sup>	52.60	21.19 ± 0.36	40.4 ± 0.8	-

<sup>#</sup>Previous measurement (unpublished 2003)

**Acknowledgments:** We thank Hayabusa2 project team and Hayabusa2 curation members. Orgueil was obtained from MNHN-Paris. This work was supported by NASA's LARS program.

#### References:

- [1] Arakawa M. et al. (2020) Science. 368, 67-71. [2] Tsuda Y. et al. (2020) Acta Astronautica. 171, 42-54. [3] Nagao K. et al. (2022) Meteor. Planet. Sci. 57, A337 #6320. [4] Nishiizumi K. et al. (2022) Lunar Planet. Sci. LIII, #1777. [5] Nishiizumi K. et al. (2022) Hayabusa Symposium 2022. S21-08. [6] Okazaki R. et al. (2022) Science. 379, eabo0431. [7] Nishiizumi K. et al. (1985) Lunar Planet. Sci. XVI, 620-621. [8] Nagao K. et al. (2023) Hayabusa Symposium 2023 (this meeting). [9] Sharma P. et al. (2000) Nucl. Instrum. Methods Phys. Res. B 172, 112-123. [10] Nishiizumi K. (2004) Nucl. Instrum. Methods Phys. Res. B223-224, 388-392. [11] Nishiizumi K. et al. (2007) Nucl. Instrum. Methods Phys. Res. B258, 403-413. [12] Yokoyama T. et al. (2022) Science. 379, eabn7850. [13] Masarik J. and Reedy R. C. (1994) Geochim. Cosmochim. Acta. 58, 5307-5317.

## Noble Gases of the 1<sup>st</sup> and 2<sup>nd</sup> AO Ryugu Samples Collected by the Hayabusa2 Spacecraft

Keisuke Nagao<sup>1\*</sup>, Kunihiko Nishiizumi<sup>2</sup>, Marc W. Caffee<sup>3</sup>, Hwayoung Kim<sup>1</sup>, Changkun Park<sup>1</sup>, Jong Ik Lee<sup>1</sup>, Jozef Masarik<sup>4</sup>  
<sup>1</sup>KOPRI, Incheon 21990, Korea, <sup>2</sup>Space Sciences Laboratory, Univ. of California, Berkeley, CA 94720-7450, USA, <sup>3</sup>Dept. of Physics & Astronomy, Purdue Univ., West Lafayette, IN 47907-2036, USA, <sup>4</sup>Comenius Univ., Bratislava, Slovakia, \*present address: Seki 2082, Maniwa-shi, Okayama 719-3156, Japan. knagao520@gmail.com

Hayabusa2 arrived at the C-type asteroid 162173 Ryugu in June 2018, and successfully collected surface samples from two sampling sites, returning ~5.4 g of samples to Earth on December 6, 2020. Surface samples stored in Chamber A were collected during the 1<sup>st</sup> touchdown (TD) on Ryugu's surface on February 21, 2019. A crater (diameter of ~14 m) on Ryugu's surface was made using a collision device - denoted "Small Carry-on Impactor (SCI)" on April 5, 2019 [1]. Samples in Chamber C were collected proximal to this artificial crater and are possibly ejecta from the north side of the crater by the 2<sup>nd</sup> TD on July 11, 2019 [2].

Our studies on the Hayabusa2 samples are based on the measurement of those nuclides produced in asteroidal surface materials by both solar (SCR) and galactic cosmic rays (GCR). Cosmic-ray-produced (cosmogenic) nuclides are used to determine the duration and nature of the exposure of materials to energetic particles [3]. Our goals are to understand both the fundamental processes on the asteroidal surface and the evolutionary history of its surface materials. These processes occur over timescales spanning the present to 10<sup>9</sup> yrs into the past, and are important not only for understanding the history of Ryugu's surface but also for studies of asteroid-meteoroid evolutionary dynamics. For Hayabusa2 samples, there are several specific questions we aim to address: (1) are the Chamber C samples, collected during the 2<sup>nd</sup> TD, ejecta deposits from the artificial crater, (2) if so, what is the original depth of each recovered sample grain in the Ryugu regolith, and (3) what is the average surface exposure time, mixing rate of regolith materials, and erosion/escape rate of Ryugu's surface? We investigate and utilize cosmogenic radionuclides (<sup>10</sup>Be, <sup>26</sup>Al, <sup>36</sup>Cl, and <sup>41</sup>Ca) and noble gases, especially cosmogenic <sup>21</sup>Ne in Ryugu samples. Expected maximum cosmogenic nuclide concentrations in millimeter-sized (~1 mg in mass) Ryugu sample are a few times 10<sup>5</sup> - 10<sup>7</sup> atoms or lower. These values are higher than the present detection limits of accelerator mass spectrometry (AMS) and noble gas mass spectrometry, but 2 orders of magnitude smaller than normal studies of cosmogenic nuclide measurements in meteoritic materials.

We present here the noble gas isotopic compositions of 6 samples (Table 1) allocated as the 1<sup>st</sup> and 2<sup>nd</sup> AO. Noble gases were measured with the system of modified-VG5400 mass spectrometer at Korea Polar Research Institute (KOPRI). The noble gas system had been used to measure the Itokawa samples at the University of Tokyo [4], and then moved to KOPRI afterward in 2015. Noble gases were extracted from each sample using a miniature furnace specially designed for small samples, using a Ta-tube with a Mo-crucible. A sample dropped into the crucible is heated from outside of the Ta-tube by a W-heater. Electric current applied to the W-heater is controlled by a computer program monitoring the heating temperature with a W-Re thermocouple. Samples were installed in a glass-made sample holder, which was set on the furnace and preheated for a day at about 120°C to remove atmospheric noble gas contamination adsorbed on the samples. Stepwise heating was applied to extract noble gases, i.e., 200, 900, and 1700°C for small samples (A0130, C0162, and C0182), and 200, 600, 900, 1200, and 1700°C for larger samples (A0221, C0012, and C0212). The extracted noble gases from each sample were purified and separated into 5 fractions, i.e., He, Ne, Ar, Kr, and Xe, then measured isotope abundances and isotopic ratios for each fraction.

Total values of concentrations of <sup>4</sup>He, <sup>20</sup>Ne, <sup>36</sup>Ar, <sup>84</sup>Kr, and <sup>132</sup>Xe, and isotope ratios of He, Ne, and Ar obtained by the stepwise heating method are presented in Table 1. Data of Orgueil CI chondrite measured in this work are also presented for comparison. Solar He and Ne with very high concentrations of <sup>4</sup>He (14.9 and 9.3×10<sup>-4</sup> cm<sup>3</sup>STP/g) and <sup>20</sup>Ne (2.0 and 1.5×10<sup>-3</sup> cm<sup>3</sup>STP/g) were observed for the aggregate samples A0221 and C0212, respectively. These samples showed <sup>20</sup>Ne/<sup>22</sup>Ne ratios of 12.8–13.7 in the temperature range of 200–900°C. The ratios are close to the value of 13.78 for solar wind (SW) [5]. Release peaks of <sup>4</sup>He for these samples were at the heating temperature of 600°C, for which <sup>3</sup>He/<sup>4</sup>He was 3.9×10<sup>-4</sup>, slightly lower than the SW value of 4.64×10<sup>-4</sup> [5]. Smaller amounts of SW He and Ne are also indicated in A0130. Neon isotopic compositions for other samples are a mixture of several primitive components, e.g., P1 (Ne-Q), P3 (presolar diamond), and Ne-E(H) (SiC) [6]. Xe isotopic ratios, e.g., <sup>130</sup>Xe/<sup>132</sup>Xe, <sup>129</sup>Xe/<sup>132</sup>Xe, and <sup>136</sup>Xe/<sup>132</sup>Xe, indicate that trapped Xe is mostly Q-Xe component, with a small or negligible contribution of cosmogenic and HL or fissiogenic Xe.

Concentrations of cosmogenic <sup>3</sup>He were difficult to calculate, because only a small excess of cosmogenic <sup>3</sup>He was observed at the low heating temperatures at 200–900°C for some samples (<sup>3</sup>He/<sup>4</sup>He = 5.2, 7.3, 4.9, and 4.8×10<sup>-4</sup> for A0221, C0012, C0162, and C0212, respectively), and most <sup>3</sup>He/<sup>4</sup>He ratios were between 1.23×10<sup>-4</sup> for trapped Q-He [6] and 4.64×10<sup>-4</sup> for SW [5]. Neon isotopic compositions are a mixture of several primitive components, e.g., SW [5], P1 (Ne-Q), P3 (presolar diamond), and Ne-E(H) (SiC) [6], to which a small contribution of cosmogenic <sup>21</sup>Ne was detected. Calculated concentrations of

cosmogenic  $^{21}\text{Ne}$  in excess of the assumed trapped  $^{21}\text{Ne}/^{22}\text{Ne} = 0.029$  are presented in Table 1. The concentrations of cosmogenic  $^{21}\text{Ne}$  are  $(4.06\text{--}11.9)\times 10^{-9}$   $\text{cm}^3\text{STP/g}$ . The concentrations of 11.9 and  $9.83\times 10^{-9}$   $\text{cm}^3\text{STP/g}$  for aggregate samples A0221 and C0212, respectively, are higher than those observed for the initial analysis samples,  $(1.6\text{--}7.8)\times 10^{-9}$   $\text{cm}^3\text{STP/g}$  [7, 8]. Exposure depths were estimated from preliminary measurements of  $^{10}\text{Be}$  and/or  $^{26}\text{Al}$  in same samples. Then, each production rate  $P_{21}$  was obtained by new calculation using the MCNP Code System. Calculated cosmic ray exposure (CRE) ages are shown in Table 1. CRE ages calculated for the samples from Chamber-A are roughly 4 and 11 Myr for A0130 and A0221, respectively. CRE ages for 3 samples from Chamber-C, C0012, C0162, and C0182, are in the range of 3–5 Myr, while C0212 has longer CRE age of 8–9 Myr. The CRE ages of 3–5 Myr for the samples from Chamber-A and -C are similar to the reported ages for initial analysis samples, 3–5 Myr [7] and ~5 Myr [8]. Contrary to these grain samples, two aggregate samples A0221 and C0212 with longer CRE ages are enriched in SW-Ne. Samples measured in the present work must have been irradiated heterogeneously by both GCR and SW on the Ryugu's surface before sampling by the Hayabusa2.

Table 1. Concentrations and isotopic ratios of noble gases <sup>1)</sup> in 6 Ryugu samples and Orgueil CI chondrite.															
Sample	Mass mg	Stepwise heating <sup>2)</sup>	<sup>4</sup> He	<sup>20</sup> Ne	<sup>36</sup> Ar	<sup>84</sup> Kr	<sup>132</sup> Xe	<sup>3</sup> He/ <sup>4</sup> He	<sup>20</sup> Ne/ <sup>22</sup> Ne	<sup>21</sup> Ne/ <sup>22</sup> Ne	<sup>38</sup> Ar/ <sup>36</sup> Ar	<sup>40</sup> Ar/ <sup>36</sup> Ar	<sup>21</sup> Ne <sub>cosm</sub>	$P_{21}$ <sup>3)</sup>	$T_{21}$ <sup>3)</sup>
			$10^{-9}\text{cm}^3\text{STP/g}$						$10^{-4}$						$10^{-9}\text{cm}^3\text{STP/g}$
A0130	0.2086	3 steps	219000	1230	1600	15.9	19.3	3.84	10.54	0.0654	0.1858	1.79	4.41	1.10–1.20	3.7–4.0
A0221	1.6610	5 steps	1490000	20400	3430	16.9	18.5	3.54	12.85	0.0362	0.1842	0.485	11.9	1.20	9.9
C0012	2.2179	5 steps	97700	472	1530	15.9	19.6	3.59	8.27	0.0978	0.1861	0.419	4.06	1.12–1.20	3.4–3.6
C0162	0.1886	3 steps	118000	706	1430	15.3	17.7	4.46	8.68	0.0984	0.1867	1.34	5.83	1.13–1.17	5.0–5.2
C0182	0.2768	3 steps	93800	432	1370	20.5	17.0	3.80	8.09	0.1280	0.1876	1.18	5.45	1.15–1.20	4.5–4.7
C0212	0.8232	5 steps	932000	15200	2720	16.1	18.7	3.89	12.95	0.0371	0.1849	0.427	9.83	1.12–1.17	8.4–8.8
Orgueil(CI)	1.7205	3 steps	672000	1130	1260	13.0	15.7	3.51	10.08	0.1099	0.1856	2.37	9.37	2.22 <sup>4)</sup>	4.22

<sup>1)</sup> Isotopic ratios of Kr and Xe are not presented.  
<sup>2)</sup> Heating temperatures are 200, 900, and 1700°C for 3 steps, and 200, 600, 900, 1200, and 1700°C for 5 steps.  
<sup>3)</sup> Each depth was estimated based on preliminary measurements of cosmogenic radionuclides. The production rates and CRE ages were not included  $\pm 5\%$  uncertainty of our new calculations and experimental errors.  
<sup>4)</sup> Production rate in  $4\pi$ -geometry for CI chondrites [9].

**Acknowledgment:** We thank Hayabusa2 project team, especially the curation members. We also thank HMNH-Paris for providing Orgueil sample.

## References

- [1] Arakawa M. et al. 2020. Science 368, 67–71
- [2] Tsuda Y. et al. 2020. Acta Astronautica 171, 42–54
- [3] Reedy R. C. et al. 1983. Annu. Rev. Nucl. Part. Sci. 33, 505–537.
- [4] Nagao K. et al. 2011. Science 26, 1128–1131.
- [5] Heber V. S. et al. 2009 Geochim. Cosmochim. Acta 73, 7414–7432.
- [6] Ott U. (2002) Noble gases in Geochem. and Cosmochem., Rev. in Mineral. Geochem. 47, 71–100.
- [7] Nagao K. et al. 2022. Meteoritical Soc. Meeting, Abstract #6134.
- [8] Okazaki R. et al. 2023. Science 379, 788.
- [9] Eugster O. 1988. Earth Planet Sci. Lett. 52, 1649–1662.

# Insights into Early Solar System Isotopic Reservoirs Inferred from Ryugu

Quinn R. Shollenberger<sup>1</sup>, Jan Render<sup>1</sup>, and Gregory A. Brennecka<sup>1</sup>

<sup>1</sup>Lawrence Livermore National Laboratory

**Introduction:** Returned primitive Solar System material presents a unique opportunity to address multiple important planetary science questions. Recent work has demonstrated that material returned from the Japan Aerospace Exploration Agency's (JAXA) Hayabusa2 mission from Cb-type asteroid (162173) Ryugu is most closely related to Ivuna-type (CI) carbonaceous chondrites [*e.g.*, 1-2], which have a chemical composition similar to that of the Sun's photosphere. The pristine nature and CI-like chemical composition of Ryugu samples allows researchers to use bulk-rock nucleosynthetic isotope anomalies to establish genetic relationships to planetary bodies and to refine our knowledge of the isotopic evolution of the Solar System, as well as the accretion history of the terrestrial planets [*e.g.*, 1-6].

The initial isotopic study of four Ryugu particles found it has an indistinguishable Fe isotope composition from CI chondrites—which is itself different from all other carbonaceous chondrites [2]. This led to the conclusion that a third isotopic reservoir may have existed in the early Solar System for CI and CI-like bodies to form separate from the carbonaceous and non-carbonaceous reservoirs. However, the existence of a third isotopic reservoir has recently been challenged through two different models [7-8], and those studies have shown that the isotopic dichotomy between carbonaceous and non-carbonaceous meteorites extends to Fe isotopes. These authors suggest that the appearance of an apparent third isotopic reservoir in the meteorite record reflects a lack of Fe isotope data from carbonaceous achondrites [8]. Here we report Fe and Ti isotopic analyses with the addition of Ni isotope compositions on a bulk sample from Ryugu to shed new light on the isotopic reservoirs present in the early Solar System.

**Methods:** Ryugu particle A0208, provided by JAXA, was analyzed in this study. This particle was part of a surface sample that was collected in Chamber A during the first touchdown of the Hayabusa2 spacecraft. Approximately 8 mg of Ryugu particle A0208 was weighed and dissolved in a pre-cleaned PFA vial using a combination of concentrated HF:HNO<sub>3</sub>, followed by aqua regia. Two procedural blanks as well as the geostandards BCR-2 and BHVO-2 were processed alongside our Ryugu sample for all procedures. Following dissolution, we obtained major and trace element concentrations using a Thermo Scientific Element XR ICP-MS at Lawrence Livermore National Laboratory (LLNL) following previously published methods [9].

All samples were processed through multiple chemical separations to purify the elements of interest using previously established procedures. The first separation was to isolate Fe from the sample matrix [10] followed by purification of Ti [*e.g.*, 11] and Ni [*e.g.*, 12]. Yields of our procedures were >80% and the blanks were negligible considering the total amount of material processed for Fe, Ti, and Ni. Iron and Ni isotopic analyses were performed on a Thermo Scientific Neptune *Plus* MC-ICPMS at LLNL while Ti isotopes were measured on a Thermo Scientific Neoma MC-ICPMS at LLNL [*e.g.*, 2, 11-12].

**Results and Discussion:** Whereas the previously analyzed Ryugu particles were all around 25 mg or less [1-2], our particle A0208 weighed only 8 mg. Despite this difference and the limited masses in general, we observe that our Ryugu particle exhibits elemental concentrations comparable to what has been reported in previous work (Fig. 1). Shown in figure 1 are major and trace element concentrations obtained for particle A0208 against the average concentration data from the initial Ryugu study [1], demonstrating overall excellent agreement. A few small differences exist between the two works (the most notable being Be), which are readily explained by heterogeneities at these small sample scales (< 25 mg).

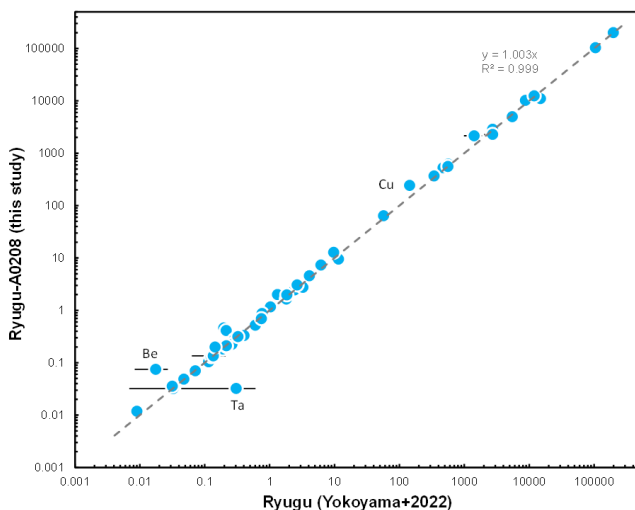
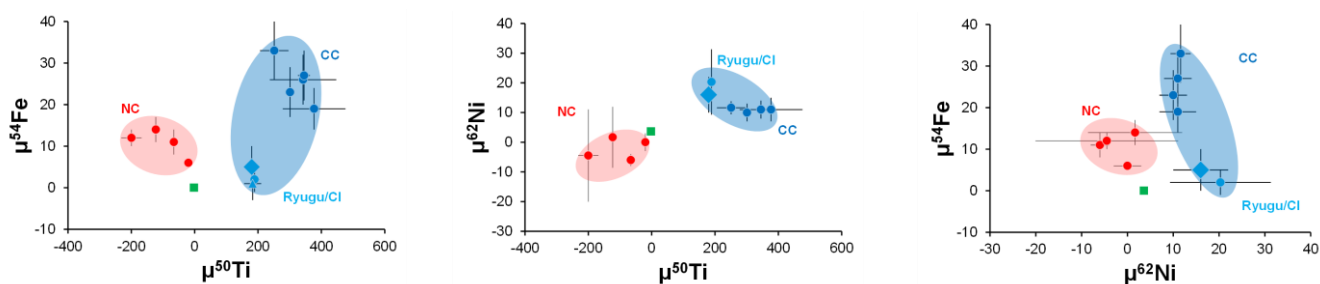


Figure 1. Major and trace element abundances of Ryugu A0208 particle of this work plotted against the average concentrations determined for Ryugu particles A0106, A0107, and C0108 from [1]. With a few exceptions, most elements are in good agreement between the two studies. Uncertainties for ICP-MS data from this study are estimated to be  $\pm 5\%$ , whereas error bars shown for data from [1] are two standard deviations of the two ICP-MS measurements reported in that work.

**Figure 1.** Major and trace element abundances of Ryugu A0208 particle of this work plotted against the average concentrations determined for Ryugu particles A0106, A0107, and C0108 from [1]. With a few exceptions, most elements are in good agreement between the two studies. Uncertainties for ICP-MS data from this study are estimated to be  $\pm 5\%$ , whereas error bars shown for data from [1] are two standard deviations of the two ICP-MS measurements reported in that work.

Shown in Figure 2 are select Ti, Fe, and Ni isotope data commonly used for genetic comparison of meteoritic materials. Our measured Fe and Ti isotopic compositions are indistinguishable from other Ryugu particles as well as from CI chondrites [1-2]. The overlapping Fe and Ti isotopic compositions of our Ryugu particle with previous measurements indicate that sample heterogeneity is not a big concern for major elements analyzed here. Although specific values and uncertainties were not provided in [13], our Ni isotope data from Ryugu particle A0208 appear to be consistent with these previous Ni isotope measurements as well as CI chondrites (Fig. 2). This result offers further support to the interpretation that Ryugu is most closely related to CI chondrites [1-2, 13].

The new Ti, Fe, and Ni isotopic data obtained in this study demonstrate that Ryugu and CI chondrites may plot on a continuation of a trend defined by the carbonaceous chondrites. Previous studies have suggested that CI chondrites and Ryugu may have formed at greater heliocentric distances compared to other carbonaceous chondrites [e.g., 2, 13-14] and our data are supportive of this interpretation given that Ryugu and CI chondrites are an endmember in the carbonaceous reservoir. While our data do not clearly provide evidence for the existence of a third isotopic reservoir in the early Solar System as previously suggested [2], this is not ruled out, either. Additional isotopic measurements are underway at LLNL for Cr and any finalized data and further interpretations will be reported at the meeting.



**Figure 2.** Plots of  $\mu^{54}\text{Fe}$  vs.  $\mu^{50}\text{Ti}$ ,  $\mu^{62}\text{Ni}$  vs.  $\mu^{50}\text{Ti}$ , and  $\mu^{54}\text{Fe}$  vs.  $\mu^{62}\text{Ni}$ , where  $\mu$  designates parts per million deviation from a terrestrial standard. Ryugu particle A0208 from this study is the large light blue diamond, previous Ryugu measurements are shown as a light blue triangle, average CI chondrite as a light blue circle, carbonaceous chondrites (CC) as dark blue circles, non-carbonaceous meteorites (NC) in red circles, and Earth as a green square. Iron and Ti isotopic data from [2]. Ni isotopic data compiled from [15-19].

**Acknowledgements:** The authors thank JAXA for providing Ryugu particle A0208 that was used in this study. This work was performed under the auspices of the U.S. DOE by LLNL with contract DE-AC52-07NA27344 with release number LLNL-ABS-848622. This work was funded by the Laboratory Directed Research and Development program of Lawrence Livermore National Laboratory (23-LW-015).

## References

- [1] Yokoyama T. et al. (2022) *Science* 10.1126/science.abn7850. [2] Hopp T. et al. (2022) *Science Advances* 8, eadd8141. [3] Fischer-Gödde M. & Kleine T. (2017) *Nature* 541, 525-527. [4] Burkhardt C. (2021) *Science advances* 7, eabj7601. [5] Schiller M. et al. (2020) *Science Advances* 6, eaay7604. [6] Burkhardt C. et al. (2019) *Geochimica et Cosmochimica Acta* 261, 145-170. [7] Marrocchi Y. et al. (2023) *The Astrophysical Journal Letters* 954, L27. [8] Yap T. & Tissot F.L.H. (2023) *Icarus* 405, 115680. [9] Wimpenny J. et al. (2022) *Earth & Planetary Science Letters* 578, 117318. [10] Rolison J. M. et al. (2019) *Applied Geochemistry* 103, 97-105. [11] Shollenberger Q. R. et al. (2022) *Geochimica et Cosmochimica Acta* 324, 44-65. [12] Render J. et al. (2018) *The Astrophysical Journal* 862, 26. [13] Spitzer F. et al. (2023) LPSC #2488. [14] Desch S.J. (2018) *The Astrophysical Journal* 238, 11. [15] Steele R.C.J. et al. (2012) *The Astrophysical Journal* 758, 59. [16] Tang H. & Dauphas N. (2012) *Earth & Planetary Science Letters* 359-360, 248-263. [17] Tang H. & Dauphas N. (2014) *Earth & Planetary Science Letters* 390, 264-274. [18] Regelous M. et al. (2008) *Earth & Planetary Science Letters* 272, 330-338. [19] Burkhardt C. et al. (2017) *Meteoritics & Planetary Science* 52, 807-826.

# Nickel isotopic composition of Ryugu and the link between CI and other carbonaceous chondrites

T. Kleine F. Spitzer<sup>1</sup>, C. Burkhardt<sup>1</sup>, the Hayabusa2-initial-analysis chemistry team, and the Hayabusa2-initial-analysis core  
<sup>1</sup>Max Planck Institute for Solar System Research, Justus-von-Liebig-Weg 3, 37077 Göttingen, Germany

The initial analyses of samples returned from Cb-type asteroid 162173 Ryugu by JAXA's Hayabusa2 mission provided isotopic, mineralogical, and chemical evidence for a close link of Ryugu to CI chondrites [1,2]. A subsequent study has shown that Ryugu and CI chondrites share the same nucleosynthetic Fe isotope signatures, which are distinct from those of other carbonaceous chondrites [6]. This not only demonstrates that Ryugu and CI chondrites are genetically linked, but also that they derive from another reservoir than all other carbonaceous chondrites [3]. However, the origin of these distinct Fe isotopic compositions of CI chondrites/Ryugu compared to other carbonaceous chondrites is not well understood. Nickel isotopes hold considerable promise to further investigate the genetic link between Ryugu and CI chondrites. When normalized to  $^{61}\text{Ni}/^{58}\text{Ni}$ , CI chondrites do not only display the largest  $\mu^{62}\text{Ni}$  and  $\mu^{64}\text{Ni}$  anomalies among carbonaceous chondrites (where  $\mu^i\text{Ni}$  is the parts-per-million deviation from terrestrial standard values), but they also have a distinct  $\mu^{60}\text{Ni}$  composition compared to all other known carbonaceous chondrite-like materials. We obtained four Ryugu samples (A0106–A0107, A0106, C0108, C0107) along with six carbonaceous chondrites including the CI chondrites Orgueil and Alais, which have been chemically processed alongside the Ryugu samples [2]. In addition, we also measured several grouped and ungrouped carbonaceous chondrites. Chemical purification of Ni involved a 3-step ion-exchange chromatographic procedure that achieves sufficiently low  $^{58}\text{Fe}/^{58}\text{Ni}$  and  $^{64}\text{Zn}/^{64}\text{Ni}$  ratios in the final purified Ni cuts to allow for accurate and precise correction of isobaric interferences. All isotope measurements were performed on the Thermo Scientific NeptunePlus MC-ICP-MS at the Institut für Planetologie, University of Münster. Instrumental mass bias is corrected by internal normalization to either  $^{61}\text{Ni}/^{58}\text{Ni}$  or  $^{62}\text{Ni}/^{61}\text{Ni}$  using the exponential law. All data are reported in the  $\mu$ -notation as the parts per  $10^6$  deviation relative to the standard.

The new Ni isotopic data for CM, CO, CV, and CR chondrites agree well with those reported in previous studies and reveal that these chondrites are characterized by negative  $\mu^{60}\text{Ni}$  and positive  $\mu^{62}\text{Ni}$  and  $\mu^{64}\text{Ni}$  values (Fig. 1). The two ungrouped carbonaceous chondrites Tagish Lake (TL) and Tarda, for which no Ni isotopic data have been reported previously, have Ni isotope anomalies similar to those carbonaceous chondrites. By contrast, CI chondrites display distinct Ni isotopic compositions and particularly distinctly larger  $\mu^{64}\text{Ni}$  and  $\mu^{60}\text{Ni}$  compared to other carbonaceous chondrites (Fig. 1). Importantly, the Ni isotopic compositions of all four Ryugu samples overlaps with those of the CI chondrites, indicating distinct Ni isotopic compositions of CI chondrites/ Ryugu compared to all other carbonaceous chondrites (Fig. 1). This is consistent with the nucleosynthetic Fe isotope variations among carbonaceous chondrites, which also reveal a uniquely distinct composition for CI chondrites and Ryugu [3].

Isotopic variations among carbonaceous chondrites are thought to reflect variable proportions of three main components having distinct isotopic compositions: refractory inclusions (e.g., CAI), chondrules/chondrule precursors, and CI chondrite-like matrix [4, 5]. The incorporation of CI chondrite-like matrix in other groups of carbonaceous chondrites is consistent with systematic variations of (i) volatile element contents, (ii) mass-dependent isotope fractionations of moderately volatile elements, and (iii) nucleosynthetic  $^{54}\text{Cr}$  anomalies with the fraction of matrix in each chondrite. However, in Ni isotope space, CI chondrites (and Ryugu) are offset from the composition of other carbonaceous chondrites, indicating that CI chondrites are not fully representative of the matrix in other groups of carbonaceous chondrites. Instead, this matrix appears to have formed from different precursor material than CI chondrites, either because it formed in a different area of the disk or because it was modified by processes in the disk prior to its incorporation in carbonaceous chondrites.

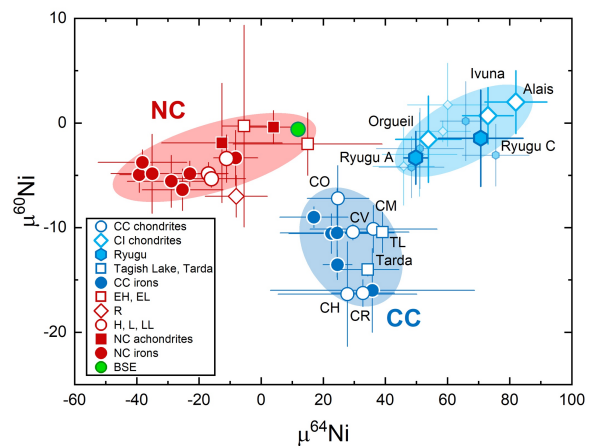


Fig. 1:  $\mu^{60}\text{Ni}$  versus  $\mu^{64}\text{Ni}$  for non-carbonaceous (NC) and carbonaceous (CC) meteorites. CI chondrites and Ryugu have distinct Ni isotopic compositions compared to NC and CC meteorites.

## References

- [1] Yada T. et al. 2022. Nature Astronomy 6:214–220.
- [2] Yokoyama T. et al. 2022. Science abn7850.
- [3] Hopp T. et al. 2022. Science Advances 8:8141.
- [4] Alexander 2019. Geochimica et Cosmochimica Acta 254:277-309.
- [5] Hellmann et al. 2023. Astrophysical Journal Letters 946: L34.

## The magnesium isotope composition of samples returned from asteroid Ryugu

Martin Bizzarro<sup>1,2\*</sup>, Martin Schiller<sup>1</sup>, Tetsuya Yokoyama<sup>3</sup> and the Hayabusa2 Initial Analysis Team

<sup>1</sup>*Centre for Star and Planet Formation, Globe Institute, University of Copenhagen, Copenhagen, K 1350, Denmark. \*email: bizzarro@sund.ku.dk*

<sup>2</sup>*Université Paris Cité, Institut de Physique du Globe de Paris, CNRS, 75005 Paris, France*

<sup>3</sup>*Department of Earth and Planetary Sciences, Tokyo Institute of Technology, Tokyo 152-8551, Japan.*

The nucleosynthetic isotope composition of planetary materials provides a record of the heterogeneous distribution of stardust within the early Solar System. Thus, nucleosynthetic signatures can be used to infer genetic relationships between early formed bodies and, ultimately, provide constraints on their accretion regions. In December 2020, the Japan Aerospace Exploration Agency Hayabusa2 spacecraft returned to Earth the first samples of a primitive asteroids, namely the Cb-type asteroid Ryugu. This provides a unique opportunity to explore the kinship between primitive asteroids and carbonaceous chondrites. Based on chemistry, mineralogy, petrology and isotope systematics of various elements, it has been proposed that Ryugu samples are closely related to Ivuna-type (CI) carbonaceous chondrites. Indeed, the bulk nucleosynthetic isotope composition for tracers like <sup>54</sup>Cr and <sup>50</sup>Ti as well as the chemical abundances of most elements are within the range of CI chondrites. Moreover, like CIs, Ryugu samples experienced extensive aqueous alteration in the presence of water and mainly consist of hydrous silicates (serpentine and saponite) and other secondary minerals (i.e., carbonate, magnetite, and sulfide) interpreted to have formed during asteroidal fluid circulation.

High-precision Mg isotope measurements can provide a novel perspective on the kinship between Ryugu with CI chondrites and, by extension, the accretion region of Cb-type asteroids. Magnesium isotope variability in Solar System materials can originate from the decay of the short-lived <sup>26</sup>Al nuclide as well as primary nucleosynthetic processes. Moreover, Mg isotopes can also be fractionated according to their masses by high-temperature events in the protoplanetary disk or, alternatively, by low-temperature parent body secondary. Thus, the combination of high-precision mass-independent and mass-dependent Mg isotope compositions is useful to understand genetic relationships and accretion history of planetary materials.

Here, we report high-precision  $\mu^{26}\text{Mg}^*$  and  $\mu^{25}\text{Mg}$  values of Ryugu samples together with those of CI, CM, CV and ungrouped carbonaceous chondrites. The stable Mg isotope composition of Ryugu aliquots define  $\mu^{25}\text{Mg}$  values ranging from  $-160\pm 20$  ppm to  $-272\pm 30$  ppm, which extends to lighter compositions relative to Ivuna-type (CI) and other carbonaceous chondrite groups. We interpret the  $\mu^{25}\text{Mg}$  variability as reflecting heterogeneous sampling of a carbonate phase hosting isotopically light Mg ( $\mu^{25}\text{Mg} \sim -1400$  ppm) formed by low temperature equilibrium processes. After correction for this effect, Ryugu samples return homogenous  $\mu^{26}\text{Mg}^*$  values corresponding to a weighted mean of  $7.1\pm 0.8$  ppm. Thus, Ryugu defines a  $\mu^{26}\text{Mg}^*$  excess relative to the CI and CR chondrite reservoirs corresponding to  $3.8\pm 1.1$  and  $11.9\pm 0.8$  ppm, respectively. These variations cannot be accounted for by in situ decay of <sup>26</sup>Al given their respective <sup>27</sup>Al/<sup>24</sup>Mg ratios. Instead, it requires that Ryugu and the CI and CR parent bodies formed from material with a different initial <sup>26</sup>Al/<sup>27</sup>Al ratio or that they are sourced from material with distinct Mg isotope compositions. Thus, our new Mg isotope data challenge the notion that Ryugu and CI chondrites share a common nucleosynthetic heritage.

# Oxygen isotope systematics of crystalline silicates in comet Wild 2: Comparison to anhydrous minerals in Ryugu and CI chondrites

Noriko T. Kita<sup>1</sup>, Mingming Zhang<sup>1</sup>, Donald E. Brownlee<sup>2</sup> and David J. Joswiak<sup>2</sup>

<sup>1</sup>*WiscSIMS, Department of Geoscience, University of Wisconsin-Madison*

<sup>2</sup>*Department of Astronomy, University of Washington*

Initial analyses of Ryugu returned samples indicated that they are similar to CI (Ivuna-type) carbonaceous chondrites, which mainly consist of minerals that formed by parent body aqueous alteration [e.g., 1-5]. Discovery of CO<sub>2</sub> bearing fluid inclusions in Ryugu pyrrhotite suggests that the Ryugu parent body accreted in the outer solar system beyond the CO<sub>2</sub> and H<sub>2</sub>O snowlines (>3-4 au [2]). Kawasaki et al. [6] conducted oxygen isotope analyses of anhydrous minerals, such as olivine and pyroxene that are extremely rare in Ryugu and CI chondrite Ivuna. They examined the distribution of mass-independent fractionation factors of oxygen 3-isotopes, expressed by  $\Delta^{17}\text{O}$  ( $= \delta^{17}\text{O} - 0.52 \times \delta^{18}\text{O}$ ), in olivine grains from Ryugu and CI chondrites, and found them to be similar to those of comet Wild 2 from the NASA Stardust mission [7-12]. They suggested that the formation region of the Ryugu asteroid could have been farther into the outer solar system than most carbonaceous chondrites and closer to the accretion region of comets.

Here, we summarize oxygen isotope data of olivine and pyroxene from comet Wild 2. To date, ~90 relatively coarse-grained particles (>2  $\mu\text{m}$  to upto 60  $\mu\text{m}$ ) have been analyzed for oxygen isotopes, including ~20 from the literature [7, 9-13] and ~70 from recent studies [14-16]. These latter studies include more than 50 particles extracted from the longest type B Stardust track (~17 mm) T227, which contains numerous relatively coarse (>2  $\mu\text{m}$  up to 20  $\mu\text{m}$ ) particles in the bulb region in addition to at least four terminal particles (TP). The largest TP measures 60  $\mu\text{m}$  in diameter and has a porphyritic chondrule-like texture [16]. The majority of Wild 2 particle analyses were conducted at the WiscSIMS IMS 1280 using a 2  $\mu\text{m}$ -sized primary beam [7, 9, 12-16]. Oxygen isotope data of individual olivine and pyroxene particles are shown in the plot of  $\Delta^{17}\text{O}$  versus Mg# (molar  $[\text{Mg}]/[\text{Mg}+\text{Fe}]$ ) in Figure 1. This diagram has been used for the studies of meteoritic chondrules to understand the isotope signatures of precursors and redox states during their formation [e.g., 17]. We also summarize published oxygen isotope analyses of olivine and pyroxene from Ryugu [6, 18] and other CI chondrites [6, 19-20] for comparison (Figure 2).

Wild 2 olivine and pyroxene show a wide range of Mg# ranging from 100 to 50 and are evenly distributed (Figure 1). The  $\Delta^{17}\text{O}$  values are bimodal where most particles are <sup>16</sup>O-poor with  $\Delta^{17}\text{O}$  values ranging from -7‰ to +7‰ and others with  $\Delta^{17}\text{O}$  of ~-22‰, values similar to CAIs in carbonaceous chondrites. The latter <sup>16</sup>O-rich particles are either LIME (low iron and Mn-enriched) olivine, nearly pure forsterite, or enstatite, all which are with highest Mg# $\geq$ 98. They are likely early solar nebula condensates similar to those in AOAs [9,12]. In addition, rare occurrences of <sup>16</sup>O-rich relict olivine have been identified, such as in the chondrule-like object Gozen-sama, studied by [7]. The <sup>16</sup>O-poor particles show a general tendency of a slight increase in  $\Delta^{17}\text{O}$  values with decreasing Mg# (Figure. 1). The majority of Wild 2 particles (60-70%) are FeO-rich (Mg#<90) and many of them show zero to slightly positive  $\Delta^{17}\text{O}$  values. Similar results have been obtained from Giant Cluster IDP U2-20GCA [21], which is considered to be of cometary origin [22]. They overlap with data from CR chondrite chondrules [16, 23-25], suggesting a genetic relationship between CR chondrites and cometary particles [e.g., 9], though FeO-rich chondrules are uncommon in CR chondrites and do not show  $\Delta^{17}\text{O}$  values higher than 1‰ [12, 16, 21].

Olivine and pyroxene data from Ryugu and CI chondrites are summarized in Figure 2. Most grains have high Mg# ( $\geq$ 98) with bimodal  $\Delta^{17}\text{O}$  values of ~-5‰ and -22‰ and minor FeO-rich grains show  $\Delta^{17}\text{O}$  values of  $\leq$ 0‰. Similar to Wild 2 particles, <sup>16</sup>O-rich olivine grains are often Mn-rich [6, 18, 20] and may be related to AOAs (e.g., [26]). However, the majority of <sup>16</sup>O-poor olivine and pyroxene in Ryugu and CI chondrites cluster at the  $\Delta^{17}\text{O}$  values of -5‰, which are uncommon among Wild 2 particles. Ryugu and CI data are more similar to chondrule data in major carbonaceous chondrites, such as CMs and CVs (e.g., [27-28]). Rare chondrule-like objects were identified in Ryugu [29], though they are substantially smaller than typical chondrules in carbonaceous chondrites.

Several Wild 2 particles are chondrule-like objects containing plagioclase and glass [7, 9-11, 16, 30]. Two of them were studied for <sup>26</sup>Al-<sup>26</sup>Mg chronology, but do not show any resolvable excess <sup>26</sup>Mg [9, 31], suggesting that they formed later than 3-4 Ma after CAI formation (by assuming homogeneity of <sup>26</sup>Al in the solar system). In contrast, the Ryugu and CI chondrite parent bodies might have accreted much earlier ~2 Ma after CAIs and experienced aqueous alteration by the heat generated from <sup>26</sup>Al decay [2]. Thus, a major difference between anhydrous minerals in comets and CI chondrites could be related to the timing of accretion in the outer solar system. Comet Wild 2 contains late-forming (>3 Ma) chondrule-like materials, which may have formed in the outer solar system [16]. They were not present in the Ryugu and CI chondrite-forming regions at the time of the CI chondrite parent body accretion.

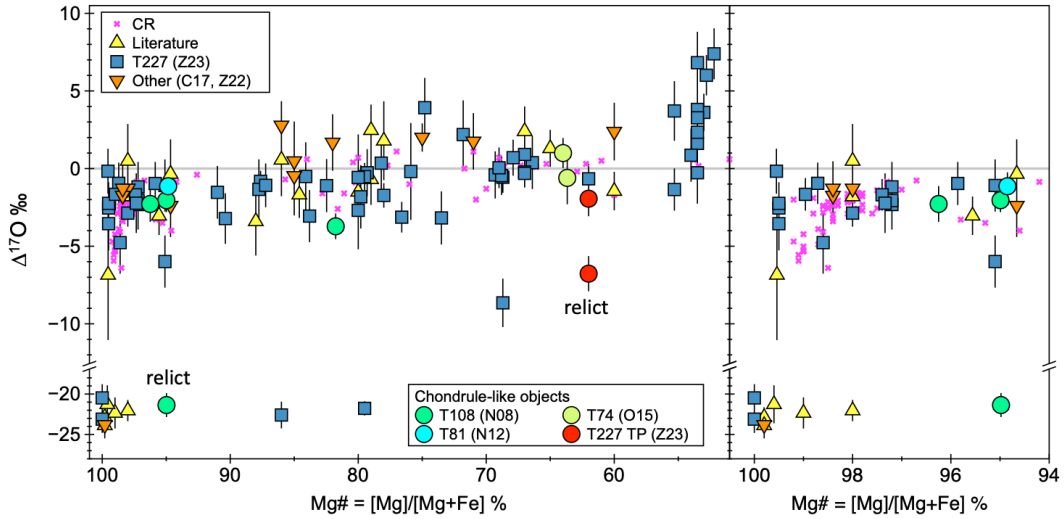


Figure 1. Mg# vs.  $\Delta^{17}\text{O}$  relationship among olivine and pyroxene particles in comet Wild 2 (after Zhang et al. [16]). Data sources: Literature [7, 9-13], T227 [16] and others [14-15]. Data from CR chondrules [17, 23-25] are plotted for comparison (error bars are ignored). Chondrule-like objects are shown as circles [7, 9, 11, 16] including  $^{16}\text{O}$ -rich relict olivine data [7, 16].

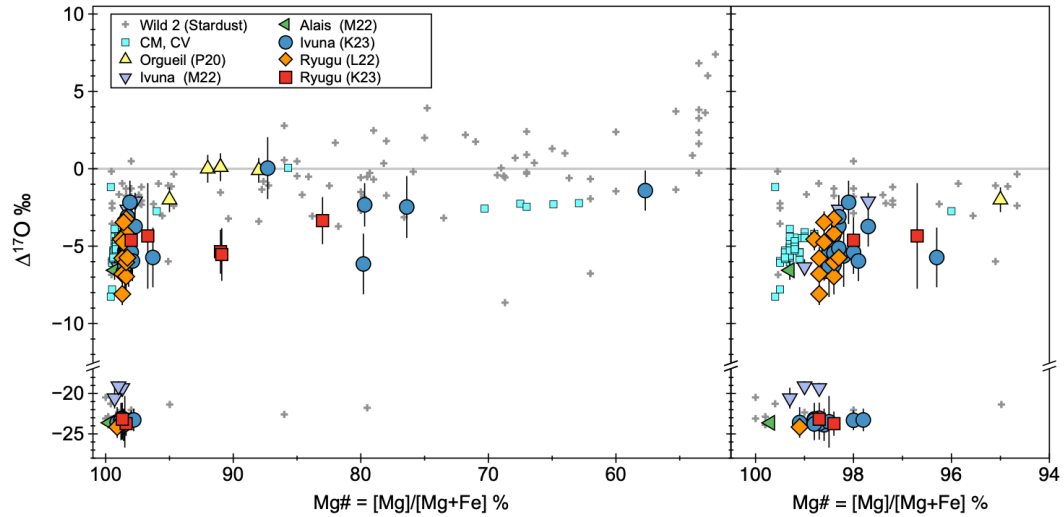


Figure 2. Mg# vs.  $\Delta^{17}\text{O}$  relationship among olivine and pyroxene grains in Ryugu (K23 [6]; L22 [18]) and CI chondrites Orgueil (P20 [19]), Ivuna (K23, M22 [20]), and Alais (M22). The Wild 2 comet data (Figure 1) and CM and CV chondrite chondrule data [27-28] are shown for comparison (error bars are ignored). Majority of  $^{16}\text{O}$ -poor Ryugu and CI chondrite data show systematically lower  $\Delta^{17}\text{O}$  and higher Mg# than those of Wild 2.

**References** [1] Yokoyama T. et al. 2023. *Science* 379:eabn7850. [2] Nakamura T. et al. 2023. *Science* 379:eabn8671. [3] Ito M. et al. 2022. *Nat. Astron.* 6:1163–1171. [4] Nakamura E. et al. 2022. *Proc. Jpn. Acad., Ser. B* 98:227–282. [5] Yamaguchi A. et al. 2022. *Nat. Astron.* 7:398–405. [6] Kawasaki N. et al. 2022. *Sci. Adv.* 8:eade2067. [7] Nakamura T. et al. 2008. *Science* 321:1664–1667. [8] Nakamura-Messenger K. et al. 2011. *MaPS* 46:1033–1051. [9] Nakashima D. et al. 2012. *EPSL* 357–358:355–365. [10] Oglione R. C. et al. 2012. *ApJ*. L745:L19. [11] Oglione R. C. et al. 2015. *GCA* 166:74–91. [12] Defouilloy C. et al. 2017. *EPSL* 465:145–154. [13] Joswiak D. J. et al. 2014. *GCA* 144:277-298. [14] Chaumard N. et al. 2018. Abstract #2163. 49th LPSC. [15] Zhang M. et al. 2022. Abstract #1057. 53rd LPSC. [16] Zhang M. et al. 2023. Abstract #. 1711. 54th LPSC. [17] Tenner T. J. et al. 2015. *GCA* 148:228-250. [18] Liu M. et al. 2022. *Nat. Astron.* 6: 1172–1177. [19] Piralla M. et al. 2020. *GCA* 269: 451-465. [20] Morin G. L. F. et al. 2022. *GCA* 332: 203-219. [21] Zhang M. et al. 2021. *EPSL* 564:116928. [22] Joswiak D. J. et al. 2017. *MaPS* 52:1612-1648. [23] Connolly H. C. and Huss G. R. 2010. *GCA* 74:2473–2483. [24] Schrader D. L. 2013. *GCA* 101:302-327. [25] Schrader D. L. 2014. *GCA* 132:50-74. [26] Mikouchi T. et al. 2022. Abstract #. 1935. 53rd LPSC. [27] Chaumard M. et al. 2018. *GCA* 228: 220-242. [28] Hertwig A. T. et al. 2018. *GCA* 224:116-131. [29] Nakashima D. et al. 2023. *Nat. Commun.* 14:532. [30] Joswiak D. J. et al. 2012. *MaPS* 47:471-524. [31] Nakashima D. et al. 2015. *EPSL* 410:54-61.

# Oxygen isotopic composition of dolomite in Ryugu: New insights into the thermal history of the Ryugu parent body.

Wataru Fujiya<sup>1</sup>, Takayuki Ushikubo<sup>2</sup>, Shingo Sugawara<sup>1</sup>, Akira Yamaguchi<sup>3</sup>, Kohei Fukuda<sup>4</sup>, Martin R. Lee<sup>5</sup>, Kentaro Terada<sup>4</sup>, Phillip A. Bland<sup>6</sup> and Bryan J. Travis<sup>7</sup>

<sup>1</sup>Faculty of Science, Ibaraki University, 2-1-1 Bunkyo, Mito, Ibaraki 310-8512, JAPAN ([wataru.fujiya.sci@vc.ibaraki.ac.jp](mailto:wataru.fujiya.sci@vc.ibaraki.ac.jp)),

<sup>2</sup>Kochi Institute for Core Sample Research, JAMSTEC, <sup>3</sup>National Institute for Polar Research, <sup>4</sup>Osaka University, <sup>5</sup>Glasgow University, <sup>6</sup>Space Science and Technology Centre, Curtin University, <sup>7</sup>Planetary Science Institute

**Introduction:** Ryugu samples underwent extensive aqueous alteration, and a variety of secondary minerals such as phyllosilicate, oxide, sulfide, and carbonate formed during water-rock interaction [1-5]. Among the secondary minerals, carbonates are of particular interest because their O and C isotopic compositions reflect the conditions of aqueous alteration, and because they can be dated using the <sup>53</sup>Mn-<sup>53</sup>Cr systematics. Previous studies of the O and C isotopic compositions of dolomite (CaMg(CO<sub>3</sub>)<sub>2</sub>) in Ryugu have suggested that it formed at temperatures lower than 80 °C [1,2,6,8] when the system was approaching equilibrium [7,8]. The <sup>53</sup>Mn-<sup>53</sup>Cr dating of Ryugu carbonate suggests that their formation may have spanned as much as 5 Myr [1,6]. Therefore, Ryugu carbonate potentially helps us decipher the thermal history of the Ryugu parent body. However, it is unclear whether Ryugu carbonate formed during prograde alteration when temperature was increasing or during retrograde cooling, which makes it difficult to establish a realistic thermal history model. In this work, we investigated the O isotopic compositions of dolomite in Ryugu samples A0203 and C0192 to further constrain its formation conditions. Also, we will measure the O isotopic compositions of magnetite in these samples to estimate the O isotopic equilibrium temperatures between dolomite and magnetite.

**Experimental:** Prior to isotope work, the microstructures of dolomite grains in samples A0203 and C0192 were characterized by Transmission Electron Microscopy (TEM) using a FEI T20 operated at 200 kV. The *in-situ* O-isotope analyses on two and six dolomite grains from A0203 and C0192, respectively, were performed using CAMECA IMS 1280-HR [9]. Negative ions of <sup>16</sup>O<sup>-</sup>, <sup>17</sup>O<sup>-</sup>, and <sup>18</sup>O<sup>-</sup>, produced by a focused Cs<sup>+</sup> primary ion beam (~30 pA, 3-4 μm in diameter), were simultaneously detected with a Faraday cup (FC) for <sup>16</sup>O<sup>-</sup> signals and two electron multipliers (EMs) for <sup>17</sup>O<sup>-</sup> and <sup>18</sup>O<sup>-</sup>. Instrumental mass fractionation was corrected using a series of dolomite-ankerite standards [10]. The uncertainties on δ<sup>17</sup>O, δ<sup>18</sup>O, and Δ<sup>17</sup>O values were typically ±1.12, ±0.86, and ±1.35‰ (2σ), respectively.

**Results and discussion:** TEM showed that dolomite grains in A0203 and C0192 differ in their crystal size and habit, with those in A0203 typically being 1-2 μm size euhedral crystals whereas C0192 dolomite is coarser and anhedral. The analyzed dolomite grains have only a small variation in δ<sup>18</sup>O values as observed by previous studies [1,6-8]. The δ<sup>18</sup>O values of A0203 and C0192 dolomite are at the higher and lower end of those reported previously and clustered at 32.91 ± 0.47‰ (N = 6; 2SE) and 26.54 ± 0.58‰ (N = 2; 2SE), respectively. Notably, the Δ<sup>17</sup>O values of A0203 and C0192 dolomite are also systematically different (-1.13 ± 0.82‰ and 0.46 ± 0.36; 2SE). A similar anti-correlation between δ<sup>18</sup>O and Δ<sup>17</sup>O values can also be recognized for the previous data, implying that Ryugu dolomite with higher δ<sup>18</sup>O values tends to have lower Δ<sup>17</sup>O values [6-8]. The Δ<sup>17</sup>O, and possibly, δ<sup>18</sup>O values of aqueous fluids are expected to have decreased during progressive aqueous alteration because of the O-isotope exchange between water and anhydrous rock which initially had higher and lower Δ<sup>17</sup>O (and δ<sup>18</sup>O) values [11,12]. Thus, the A0203 dolomite with lower Δ<sup>17</sup>O values likely precipitated from more evolved fluids that underwent O-isotope exchange to a greater extent than the C0192 dolomite. On the other hand, the equilibrium O isotopic fractionation between water and dolomite is larger at lower temperatures with the δ<sup>18</sup>O values of dolomite being higher than those of water [13]. Therefore, the A0203 dolomite with higher δ<sup>18</sup>O values likely precipitated at lower temperatures than the C0192 dolomite. These observations may suggest that Ryugu dolomite formed during retrograde cooling. This argument is in line with the small variation in δ<sup>13</sup>C values observed for Ryugu dolomite, which suggests its formation in higher O fugacity at the later stage of aqueous alteration [7]. For further information regarding the formation conditions of dolomite, we plan to measure the <sup>53</sup>Mn-<sup>53</sup>Cr ages of dolomite in A0203 and C0192.

## References:

- [1] Yokoyama T. et al. 2022. Science 379: eabn7850. [2] Nakamura E. et al. 2022. Proc. Jpn. Acad., Ser. B 98: 227-282. [3] Ito M. et al. 2022. Nat. Astron. 6: 1163-1171. [4] Nakamura T. et al. 2022. Science 379: eabn8671. [5] Yamaguchi A. et al. 2023. Nat. Astron. 7: 398-405. [6] McCain K. A. et al. 2023. Nat. Astron. 7: 309-317. [7] Fujiya W. et al. 2023. Nat. Geosci. 16: 675-682. [8] Kita N. T. et al., submitted. [9] Fujiya W. et al. 2020. Geochim. Cosmochim. Acta 274: 246-260. [10] Śliwiński, M. G. et al. 2016. Geostand. Geoanal. Res. 40: 157-172. [11] Clayton & Mayeda 1984. Earth Planet. Sci. Lett. 67: 151-161. [12] Marrocchi et al. 2018. Earth Planet. Sci. Lett. 482: 23-32. [13] Zheng Y.-F. et al. 1999. Geochem. J. 33: 109-126.

# Numerical Simulation of Ryugu’s Thermophysical Properties using the Discrete Element Method

B. Agrawal<sup>1</sup>, M. Grott<sup>1</sup>, J. Knollenberg<sup>1</sup>, J. Biele<sup>2</sup>, B. Gundlach<sup>3</sup>, J. Blum<sup>4</sup>

<sup>1</sup>German Aerospace Center, Berlin, Germany, <sup>2</sup>German Aerospace Center, Köln, Germany, <sup>3</sup>Westfälische Wilhelms-Universität Münster, Germany, <sup>4</sup>Technische Universität Braunschweig, Germany

Between June 2018 and November 2019, the Hayabusa2 mission [1] investigated the near-Earth asteroid (162173) Ryugu. The main objective of the mission was to study this pristine C-type asteroid to better understand the origin and evolution of materials in the early solar system. Hayabusa2 deployed the MASCOT lander in October 2018 and following a detailed remote sensing and in-situ investigation, Hayabusa2 returned samples to Earth in December 2020. A summary of main findings of the mission was recently reviewed by [2], who also compared results obtained during the remote sensing, in-situ, and sample analysis phases.

The detailed study of Ryugu over scales ranging from the micro (sample) scale to global remote sensing data revealed that while several properties derived from remote sensing and in-situ analysis agree very well with results obtained from the sample analysis, some discrepancies exist [2]. These scale dependent effects include properties like reflectance and thermophysical properties. Here, we focus on the derived thermal properties, which were determined using MASCOT’s MARA radiometer [3], the Hayabusa2 orbiter’s TIR thermal infrared imager [4], as well as the returned samples [5]. While in-situ and remote sensing data roughly agree, yielding thermal inertias of  $282_{-25}^{+93} \text{ Jm}^{-2}\text{K}^{-1}\text{s}^{-1/2}$  [6, 7] and  $225 \pm 45 \text{ Jm}^{-2}\text{K}^{-1}\text{s}^{-1/2}$  [4, 8], respectively, sample analysis indicates values of  $890 \pm 45 \text{ Jm}^{-2}\text{K}^{-1}\text{s}^{-1/2}$  [5], which are thus about three times as large.

The reason for the observed scale dependence of the thermophysical properties remains unknown, but it has been proposed that the difference could be caused by a thermal shielding effect on intermediate scales [5]. Cracks may, for example, be generated by thermal fatigue and a conceptual model of how these cracks may be distributed inside boulders is shown in the left panel of Fig. 1. Thermal fatigue would extend to a few skin depths  $d_c = \sqrt{\kappa P/\pi}$ , where  $\kappa = k/\rho c_p$  is thermal diffusivity,  $\rho$  is density,  $c_p$  is specific heat, and  $P$  is the period of the forcing (a day-night cycle). Remote sensing instruments like MARA and TIR are sensitive to material over a similar depth range, while samples could contain considerably less cracks.

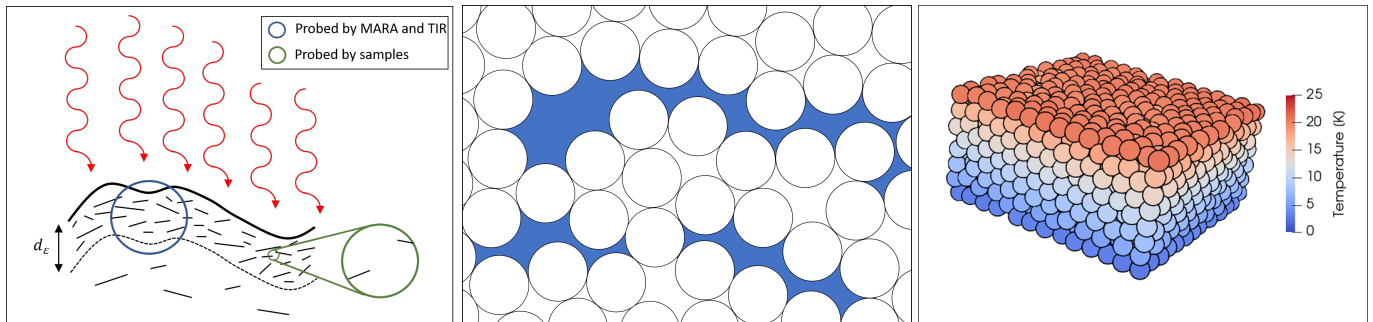


Figure 1: Left: Conceptual model of scale dependence of thermophysical properties. The range of materials sampled by the in-situ and remote sensing instruments MARA and TIR is indicated in blue, while the returned samples are indicated in green. On large scales, the material may exhibit abundant cracks due to insolation induced fatigue, while samples may contain only few cracks. Middle: Modeling approach including cracks induced by thermal fatigue using discrete elements. Fatigue induced cracks separating particles are indicated in blue. Right: First results of simulating heat flow through a bed of monodisperse particles without cracks. Colour represents particle temperatures going from red (hot) to blue (cold).

Our project focuses on exploring this discrepancy and formulating a thermophysical model of the boulders including cracks and sintering. To understand the thermophysical properties of asteroids, we base our model on the LIGGGHTS(R)-PUBLIC package [9]. It is an open source discrete element method particle simulation software built for simulating general granular motion and atomic/molecular dynamics. The program integrates Newton’s equations of motion for a large collection of spherical particles which interact via short or long range forces. The inter-particle forces are determined based on a user selected contact model which can encompass interactions such as elastic (contact) forces, rolling friction, cohesion and surface geometry of particles. In addition to mechanical interactions, the package can also be used to study the thermal energy transport between particles in contact. This is governed by

the thermal conductivities of the particles and their contact areas. Here we specify contact areas as the cross section of the geometrical overlap of two spherical particles. Upon introducing cracks in a random packing of monodisperse particles (middle panel in Fig. 1), we intend to study the thermal properties of the bulk material.

As a benchmark test for the numerical code we calculate the steady-state heat flow through a particle-bed to reproduce the relation between thermal conductivity, contact areas, and particle radii. Once in thermal equilibrium, thermal conductivity of the bed can be calculated given the specified temperature boundary conditions and resulting heat flux through the bed. This can then be compared to analytical and experimental results for monodisperse particles [10]. First results of the simulation are shown in the right hand panel of Fig. 1 where heat is flowing vertically downwards through a bed of cohesion-less particles with adiabatic boundary conditions elsewhere.

Once the numerical method has been benchmarked using monodisperse cohesion-less particles, we will include polydisperse particles and a parameterized description of enhanced heat transport through inter-particle bonds. Using the contact area as a tuning parameter we fit the numerical results to the thermal properties, as derived from sample analysis [5]. Then, cracks will be introduced as outlined in the middle panel of Fig. 1 and the associated reduction in thermal conductivity will be investigated. In this way, we will systematically study the amount of material disruption necessary to match the remote sensing observations [7, 6, 4].

## References

- [1] Sei-ichiro Watanabe et al. In: *Space Science Reviews* 208.1 (July 2017), pp. 3–16.
- [2] Katharina Otto et al. In: *Earth, Planets and Space* 75.1 (Apr. 2023), p. 51.
- [3] M. Grott et al. In: *Space Science Reviews* 208.1 (July 2017), pp. 413–431.
- [4] Tatsuaki Okada et al. In: *Nature* 579.7800 (Mar. 2020), pp. 518–522.
- [5] T. Nakamura et al. In: *Science* 379.6634 (2023), eabn8671.
- [6] Maximilian Hamm et al. In: *Planetary and Space Science* 159 (2018), pp. 1–10.
- [7] M. Grott et al. In: *Nature Astronomy* 3.11 (Nov. 2019), pp. 971–976.
- [8] Yuri Shimaki et al. In: *Icarus* 348 (2020), p. 113835.
- [9] Christoph Kloss et al. In: *Progress in Computational Fluid Dynamics* 12.2-3 (2012), pp. 140–152.
- [10] N. Sakatani et al. In: *AIP Advances* 7.1 (Jan. 2017), p. 015310.

# Defect and exsolution microstructures in four pyroxene-rich grains from Itokawa

Falko Langenhorst<sup>1,2</sup>, Agnese Fazio<sup>1</sup>, and Dennis Harries<sup>3</sup>

<sup>1</sup>*Analytical Mineralogy of Nano- and Microstructures, Institute of Geoscience, Friedrich Schiller University Jena, Germany*

<sup>2</sup>*Hawai'i Institute of Geophys. and Planetology, School of Ocean and Earth Science and Technology, University of Hawai'i at Manoa, USA*

<sup>3</sup>*European Space Resources Innovation Centre, Luxembourg Institute of Science and Technology, 41 rue du Brill, L-4422Belvaux, Luxembourg*

**Introduction:** In 2010, the Hayabusa spacecraft returned precious regolith grains from the rubble pile asteroid 25143 Itokawa. Subsequent investigations confirmed the link between LL4-6 ordinary chondrites and the S-type asteroid Itokawa and revealed its eventful past [1, 2]. The processes reported in regolith grains comprise thermal annealing in the original parent body and the full range of space weathering effects from surface amorphization by ion bombardment to collisional fragmentation [2-6]. Pyroxenes, the second most abundant phase in ordinary chondrites, are an important source of information on these processes, as they develop various process-indicative defects. Thus, we pursued here a systematic study of the microstructures in ortho- and clinopyroxene grains from Itokawa and discuss the results in terms of thermal metamorphism and space weathering.

**Samples and methods:** In the context of the 4th International Announcement of Opportunity for Hayabusa sample investigation, we have obtained four pyroxene-containing Itokawa particles: RB-QD04-0092, RA-QD02-0205, RB-CV-0192, and RB-CV-0144 [7]. These grains were cut by focused ion beam (FIB) preparation on a scanning electron microscope (SEM) and then studied by analytical transmission electron microscopy (TEM), following the procedure described by [6].

**Results:** *RB-QD04-0092* is a flat grain (29 x 26 x 12  $\mu\text{m}$ ) consisting of orthopyroxene ( $\text{En}_{78}\text{Fs}_{21}\text{Wo}_1$ ) and olivine ( $\text{Fo}_{71-78}$ ). Both olivine and orthopyroxene show defects that are compatible with local shock metamorphism, i.e. olivine contains [001] dislocations, while orthopyroxene is pervaded by multiple (100) clinoenstatite lamellae. The regolith grain shows a 40-70 nm wide continuous damaged rim due to solar wind irradiation.

*RA-QD02-0205* is a prismatic grain (55 x 43 x 15  $\mu\text{m}$ ) that only consists of a single crystal orthopyroxene ( $\text{En}_{74}\text{Fs}_{24}\text{Wo}_2$ ). The dominant defects are also pervasive (100) clinoenstatite lamellae, which are decorated by partial dislocations. The grain is surrounded by a 50 nm thin polynanocrystalline rim.

*RB-CV-0192* is also prismatic in shape (19 x 10 x 8  $\mu\text{m}$ ), and contains both orthopyroxene ( $\text{En}_{76}\text{Fs}_{23}\text{Wo}_1$ ) and clinopyroxene ( $\text{En}_{50}\text{Fs}_7\text{Wo}_{43}$ ). Adjacent olivine, plagioclase, and whitlockite were detected, too. Besides (100) clinoenstatite lamellae in orthopyroxene there are no other defects. The solar wind damaged polynanocrystalline rim is up to 50 nm thick.

*RB-CV-0144* is 17 x 12 x 5  $\mu\text{m}$  in size and contains both orthopyroxene ( $\text{En}_{79}\text{Fs}_{20}\text{Wo}_1$ ) and clinopyroxene ( $\text{En}_{50}\text{Fs}_6\text{Wo}_{44}$ ). The pyroxenes possess subgrain boundaries and are traversed by thin (up to 10 nm) (100) exsolution lamellae. One side of the entire regolith grain displays a polynanocrystalline and layered rim of up to 60 nm thickness.

**Discussion:** The presence of amorphous to nanocrystalline rims documents the solar wind damage of Itokawa grains. Moreover, the occurrence of shock defects in localized areas of olivine and pyroxenes (clinoenstatite lamellae and dislocations) as well as the absence of microcraters on their surfaces indicate that cascades of collisions took place in the regolith. As consequence of active space gardening the effective exposure time of regolith grains must have been reduced. Of particular interest is the observation of thin exsolution lamellae in pyroxene, whose width of up to 10 nm points to slow cooling rates of  $< 1$   $^{\circ}\text{C}$  per 1000 years at peak temperatures of  $800^{\circ}\text{C}$  [2, 8].

**Acknowledgements:** We thank JAXA for providing access to the Itokawa particles. FIB-TEM facilities at FSU Jena were funded by the Gottfried-Wilhelm-Leibniz award to FL (LA 830/14-1). AF is grateful to the Alexander von Humboldt Foundation for a postdoctoral grant.

## References

- [1] Noguchi T., et al. 2011 Science 333:1121. [2] Nakamura T. et al. 2011 Science 333:1113. [3] Keller L.P. and Berger E.L. 2014 Earth Planets and Space 66:71. [4] Noguchi T., et al. 2014 Meteoritics & Planetary Science 49:188. [5] Harries D. and Langenhorst F. 2014 Earth Planets and Space 66:163. [6] Langenhorst F., et al. 2014 Earth Planets and Space 66:118. [7] Fazio et al. 2020 Vol.14, EPSC2020-645. [8] Weinbruch S. and Müller W.F. 1995 Geochimica et Cosmochimica Acta 59: 3221.

## Asteroid Itokawa ... but when did form exactly?

F. Jourdan<sup>1</sup>, N.E. Timms<sup>1</sup>, T. Nakamura<sup>2</sup>, W.D.A. Rickard<sup>1</sup>, C. Mayers<sup>1</sup>

<sup>1</sup>*Curtin University, Perth, GPO Box U1987, WA, Australia*

<sup>2</sup>*Tohoku University, Aoba, Sendai, Miyagi 980-8578, Japan*

Rubble pile asteroids consist of reassembled fragments from shattered monolithic asteroids and are much more abundant than previously thought in the solar system. In earlier studies (*1, 2*), we analysed five regolith dust particles recovered by the Hayabusa space probe from the rubble pile asteroid 25143 Itokawa, using a workflow of microstructural analysis by electron backscatter diffraction (EBSD), element mapping by time-of-flight secondary ion mass spectrometry (ToF-SIMS  $\pm$  atom probe) and  $^{40}\text{Ar}/^{39}\text{Ar}$  geochronology. We showed that Itokawa must have formed before or at ca.  $\geq 4.2$  Ga and concluded that rubble pile asteroids can survive ambient solar system bombardment processes for extremely long periods. Here, we continue our quest to understand the bombardment history of Itokawa with the so far seemingly elusive goal of precisely pinpointing the age and nature of the catastrophic breakup of Itokawa's parent body. Only through a larger number of  $^{40}\text{Ar}/^{39}\text{Ar}$  ages on single particles and U/Pb ages on phosphate grains (*3*) coupled with careful particle characterizations, will we be able to achieve this goal. With that in mind, we analysed three new particles.

RA-QD02-0300 (dia. = 190  $\mu\text{m}$ ) is composed of olivine, plagioclase, with minor troilite. EBSD and ToF-SIMS analyses show that the plagioclase in this particle is distributed in vein-like structures and has a fine polycrystalline texture of  $<10$   $\mu\text{m}$  grains with abundant inclusions and K-rich exsolutions. This suggests it represents recrystallised melt domains. Olivine crystals show no sign of shock deformation. We obtained a plateau age of **4130  $\pm$  33 Ma** ( $P = 0.55$ ). Noticeably, this age is very similar to previous results from other particles at  $4219 \pm 35$  and  $4149 \pm 41$  Ma (*1*), indicating an age concentration around that time. Could it be that the parent body of Itokawa broke up at ca. 4.2 Ga while some of the impact heated material slowly cooled down inside the newly formed insulating rubble pile asteroid over ca. 100 million years? This scenario is tantalizing as it would be similar to the scenario proposed by (*4*) for the breakup of an initially hot chondritic parent body at 4.5 Ga and with subsequent debris cooling at rates of ca. 1 to 10  $^{\circ}\text{C}/\text{Ma}$  inside the rubble pile asteroids.

RA-QD02-0306 (160  $\mu\text{m}$ ) is composed of olivine and plagioclase with minor troilite and chromite. This particle is the only  $^{40}\text{Ar}/^{39}\text{Ar}$ -dated particle which contains measurable solar wind, with a  $^{38}\text{Ar}/^{36}\text{Ar}$  ratio of  $0.188 \pm 0.049$  ( $2\sigma$ ) that is indistinguishable from modern solar wind value. Along with the presence of abundant micro-craters, melt drop and blisters observed on the surface of the particle observed by (*5*), this indicates that this particle spent some time directly at the surface of the asteroid. This particle shows a structured  $^{40}\text{Ar}/^{39}\text{Ar}$  age spectrum, with two different portions attributed to the gas released by the plagioclase and olivine phases. Plagioclase yielded a mini-plateau (59 %  $^{39}\text{Ar}$  released) age of **4557  $\pm$  61 Ma** ( $P = 0.71$ ) similar to the U-Pb phosphate age of  $4640 \pm 360$  Ma obtained by (*3*) on another particle, suggesting that it recorded the initial cooling deep inside Itokawa's parent asteroid and was not affected by heat during the breakup process. This demonstrates that, during the breakup of Itokawa's parent body, part of the asteroid experienced minimum to negligible shock pressure and temperature increase. This is similar to the conclusions reached via impact modelling calculated for the rubble pile asteroid Ryugu (*6*). This is also in excellent agreement with breakup models of structurally weakened monolith asteroids that do not require a particularly large impactor to shatter (*7*).

RA-QD02-0311 (108  $\mu\text{m}$ ) is composed of olivine, Ca-rich pyroxene, plagioclase and troilite. Elemental maps show that this particle contains very little plagioclase compared to the other particles and most of the K is contained in a rim-like structure exposed at the edge of the particle. Olivine crystals show no sign of shock deformation, yet  $^{40}\text{Ar}/^{39}\text{Ar}$  dating reveals a complex age spectrum with maximum weighted-mean age of  $705 \pm 53$  Ma ( $P=0.39$ ) including 47% of  $^{39}\text{Ar}$  released and indicating an impact  $\leq 0.7$  Ga. This maximum age, coupled

with an available impact age of  $2291 \pm 139$  Ma (2) and maximum age estimates (1, 8), suggests that impact events happened many times during the history of Itokawa and that the high porosity of the rubble pile material was able to convert low-shock events into high temperature spikes, sufficient to reset and/or partially reset the  $^{40}\text{Ar}/^{39}\text{Ar}$  chronometer (2) in some material.

In summary, we propose that Itokawa's parent body was disrupted ca. 4.2 billion years ago in a process involving heterogenous temperature distribution during the impact. Some of the heated material, mixed with cold material, cooled down inside a larger version of Itokawa, possibly over a period of ca. 100 Ma. Itokawa kept being bombarded and eroded by small impactors since its formation with some of these events recorded by the  $^{40}\text{Ar}/^{39}\text{Ar}$  system.

## References

[1] Jourdan et al. 2023. *Proceedings of the National Academy of Sciences* **120**, e2214353120. [2] Jourdan et al., 2017. *Geology* **45**, 819-822. [3] Terada et al., 2018. *Scientific Reports* **8**, 11806. [4] Lucas et al., 2020. *Geochim Cosmochim Acta* **290**, 366-390. [5] Matsumoto et al., 2018. *Icarus* **303**, 22-33. [6] Nakamura et al., 2022. *Science* **379**, eabn8671. [7] Michel et al. 2004. *Icarus* **168**, 420-432. [8] Park et al., 2015. *Meteoritics and Planetary Science* **50**, 2087-2098.

# Characterization of a mass movement site in Benu’s Bralgah Crater and implications for other asteroids

Yuhui Tang<sup>1</sup>, D.S. Lauretta<sup>1</sup>, R.-L. Ballouz<sup>2</sup>, D.N. DellaGiustina<sup>1</sup>, C.A. Bennett<sup>1</sup>, D.R. Golish<sup>1</sup>

<sup>1</sup>*Lunar and Planetary Laboratory, University of Arizona, Tucson, AZ, USA.*

<sup>2</sup>*The Johns Hopkins University Applied Physics Laboratory, Laurel, MD, USA.*

Near-Earth asteroids such as Benu and Ryugu have boulder-covered surfaces and latitude-dependent slope distributions, signifying that mass movements of boulders perform significant roles in the surface evolution of these small bodies. The OSIRIS-REx (Origins, Spectral Interpretation, Resource Identification, and Security–Regolith Explorer) mission [1] documented numerous locations on Benu exhibiting evidence of mass movements of surface material, mostly towards the lower elevation equatorial region [2]. One such location, contained within Bralgah Crater, was considered (but not used) by the mission as a candidate site for sample collection; thus, high-resolution images collected during reconnaissance of this area allow a more detailed survey than would be possible elsewhere [3] [Fig. 1]. An apparent flow “wake” downhill from a 4.8-m-diameter central boulder in the area, where medium-sized boulders are much less prevalent than in the surrounding terrain, provides an opportunity to investigate the characteristics of mass flow on the asteroid. Through boulder mapping and topographic analysis, we found evidence of a pileup behind the central boulder, as well as a strong orientational preference of the boulders in this area [Fig. 2]. This preferential long-axis orientation exhibits the same westward deflection from the expected downslope direction that we observed at another mass movement site in Benu’s northern hemisphere [4], implying that a global mechanism with effects mirrored between the northern and southern hemispheres is affecting the mass flows.

We performed dynamical simulations of seismic shaking using the discrete-element N-body code PKDGRAV [5–8] to better constrain the conditions that may have formed the landscape. In these simulations, we used boulder sizes similar to those surveyed at the Bralgah Crater site and an environment with a similar 4.8-m-diameter central boulder. We were able to replicate the pileup of material uphill from the central boulder and the wake downhill from it, producing similar elevation profiles created by a lack of downflowing material in the wake area [Fig. 3].

Simulations also showed a preferential orientation emerging, with a strong possibility for preferential orientation parallel to direction of motion. Combined with the orientational preference observed in this and other studies of Benu’s landscape, this indicates that the Coriolis effect could be a major factor in the mass movement of boulders and would help to explain the westward deflection of the boulders’ long-axis orientation. Numerical simulations show that the Coriolis effect is strong enough to induce an east-west displacement of the boulders, which can amount to 10% of the downslope displacement, which could lead to the observed orientational preferences. This effect would be expected to occur on other fast-spinning asteroids, such as Ryugu, where this hypothesis predicts a similar orientational preference, with eastward deviation from the poleward migration of the boulders.

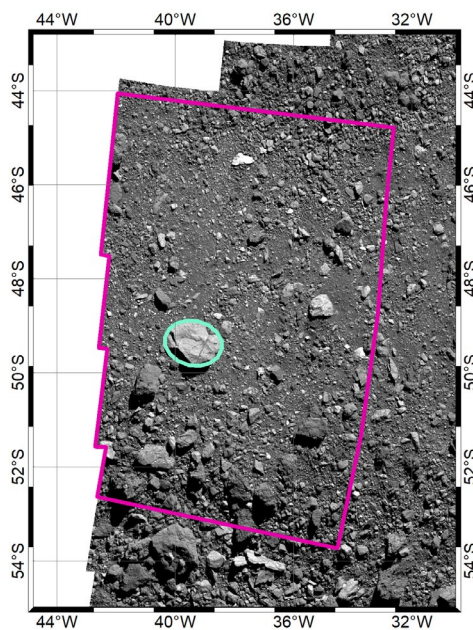


Figure 1. A map of the survey area (magenta outline) within Bralgah Crater, projected in ArcGIS, with the central boulder (long axis, 4.8 m) highlighted by the light blue best-fit ellipse. The downhill direction is north in this area.

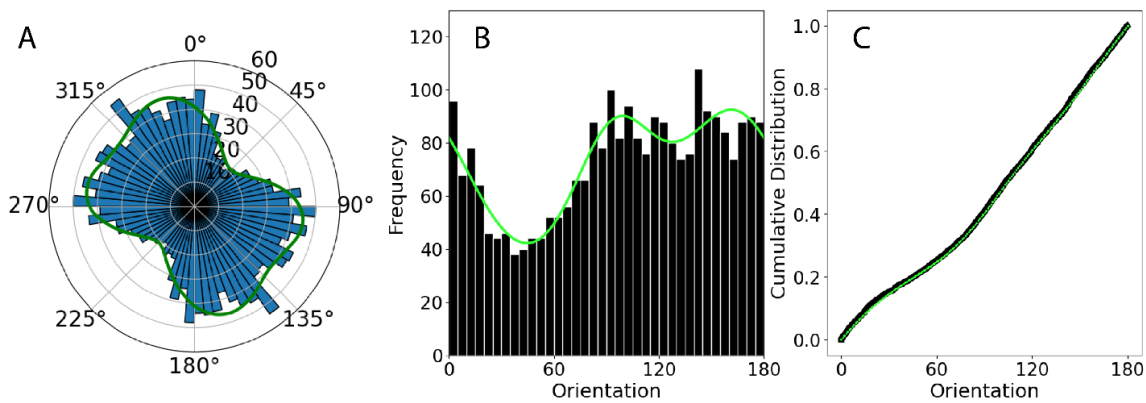


Figure 2. Orientations of the surveyed boulders as a rose diagram (A) and histogram (B), with the data best fitted by a bimodal von Mises distribution (green) with peaks at  $94.1^\circ$  and  $164.2^\circ$  ( $p$ -value = 0.839). (C) The empirical distribution function (black line) and cumulative distribution function (green line) of the orientations, used for the K-S tests to derive the  $p$ -values.

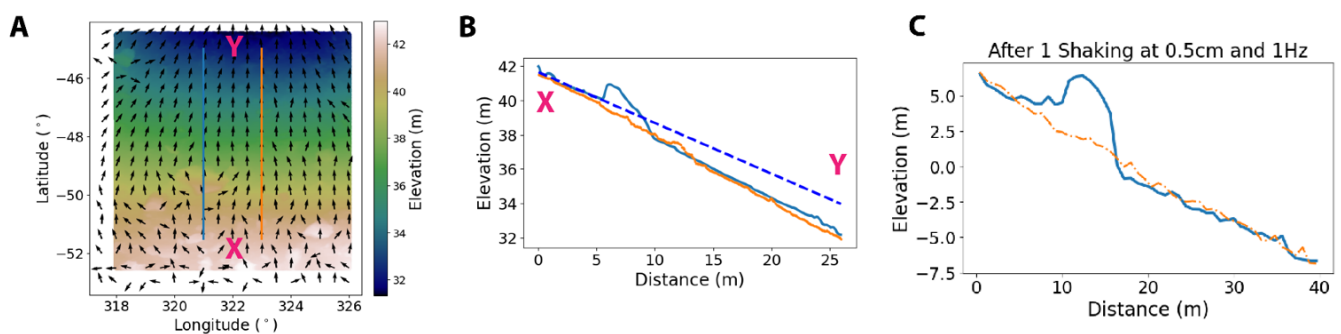


Figure 3. (A) Elevation map of the study site, overlaid with arrows indicating the direction of greatest slope, with the locations of the elevation profiles along longitudes  $321^\circ\text{E}$  and  $323^\circ\text{E}$  marked in cyan and orange, respectively. (B) The elevation profiles indicated in (A), with the  $321^\circ\text{E}$  line profile (cyan) crossing the middle of the central boulder. The blue dashed line represents the best-fit slope of the pileup area uphill from the central boulder, extrapolated across the entire mass movement length. The extrapolated profile ranges from 0.8 to 1.6 m above the actual elevation profile downhill from the central boulder, with greater differences further north (downhill). (C) Elevation profile of simulations after one shaking. The cyan solid line shows elevation along the center of the wake, and the orange dashed-dot line shows the elevation along a parallel transect away from the wake.

## References

- [1] Lauretta, D. S., et al. (2017). OSIRIS-REx: Sample Return from Asteroid (101955) Bennu. *Space Science Reviews*, 212(1–2), 925–984. <https://doi.org/10.1007/s11214-017-0405-1>
- [2] Jawin, E. R., et al. (2020). Global Patterns of Recent Mass Movement on Asteroid (101955) Bennu. *Journal of Geophysical Research: Planets*, 125(9). <https://doi.org/10.1029/2020JE006475>
- [3] Lauretta, D. S., et al. (2021). OSIRIS-REx at Bennu: Overcoming challenges to collect a sample of the early Solar System. In *Sample Return Missions* (pp. 163–194). Elsevier. <https://doi.org/10.1016/B978-0-12-818330-4.00008-2>
- [4] Tang, Y., et al. (2023). Simulating impact-induced shaking as a triggering mechanism for mass movements on Bennu. *Icarus*, 395, 115463. <https://doi.org/10.1016/j.icarus.2023.115463>
- [5] Ballouz, R.-L. (2017). Numerical Simulations of Granular Physics in the Solar System [Ph.D., University of Maryland, College Park].
- [6] Richardson, D. C., Quinn, T., Stadel, J., & Lake, G. (2000). Direct Large-Scale N-Body Simulations of Planetesimal Dynamics. *Icarus*, 143(1), 45–59. <https://doi.org/10.1006/icar.1999.6243>
- [7] Schwartz, S. R., Richardson, D. C., & Michel, P. (2012). An implementation of the soft-sphere discrete element method in a high-performance parallel gravity tree-code. *Granular Matter*, 14(3), 363–380. <https://doi.org/10.1007/s10035-012-0346-z>
- [8] Zhang, Y., et al. (2017). Creep stability of the proposed AIDA mission target 65803 Didymos: I. Discrete cohesionless granular physics model. *Icarus*, 294, 98–123. <https://doi.org/10.1016/j.icarus.2017.04.027>

# Photometry of Ryugu and SCI crater as inferred by ONC images

A. Longobardo<sup>1</sup>, M. Angrisani<sup>1</sup>, E. Palomba<sup>1</sup>, F. Dirri<sup>1</sup>, Y. Yokota<sup>2</sup>, T. Kouyama<sup>3</sup>, R. Honda<sup>4</sup> and the Hayabusa2/ONC Team

<sup>1</sup> INAF-IAPS, via Fosso del Cavaliere 100, 00133 Rome, Italy

<sup>2</sup> JAXA-ISAS, 3-1-1 Yoshinodai, Chuo-ku, Sagami-hara City, Kanagawa Prefecture, 252-5210, Japan

<sup>3</sup> National Institute of Advanced Industrial Science and Technology, Umezono 1-1-1, Tsukuba, 305-8568, Japan;

<sup>4</sup> Kochi, University, Kochi, Japan

The JAXA/Hayabusa2 rendezvoused with the Ryugu asteroid from June 2018 to November 2019, performing an artificial impact experiment on 5<sup>th</sup> April 2019.

The goal of this work is to study the photometric properties' variation of the target area (latitude 4.5-10°N; longitude 299-305°E) after the artificial impact experiment. This is done by applying an empirical method based on the statistical analysis of the ONC camera's dataset (in particular, the  $v$  band, centred at 0.55  $\mu\text{m}$ ), similar to that applied to several asteroids (e.g., Longobardo et al., 2014; 2018) and to the NIRS3 dataset of Ryugu (Longobardo et al., 2022).

The method has been firstly applied on the entire dataset acquired between March and April 2019, covering most of the Ryugu surface. The first step was the retrieval of the equigonal albedo, by applying the Akimov disk function. The obtained equigonal albedo is independent of incidence and emission angle when phase angle is lower than 60°, while a slight dependence is still present for larger phase angles.

Then, the average phase function of Ryugu was obtained. This is very similar to that obtained on the NIRS3 dataset (i.e., in a different spectral range), according to our expectations.

Then, we calculated two photometric parameters  $R20$  (i.e., the radiance factor at 20° phase) and  $PCS_{1540}$  (i.e., the phase function steepness between 15° and 40° phase angles) and compared them to photometric parameters calculated on phase functions of other asteroids visited by space missions and on both disk-integrated and disk-resolved phase functions of Ryugu obtained by Tatsumi et al. (2019). The disk-resolved phase functions by Tatsumi et al. (2019) and obtained in this work are in good agreement.

Nevertheless, the Ryugu's disk-resolved phase function is much flatter than other dark asteroids. Otherwise, the disk-integrated phase function of Ryugu is in good agreement with other dark asteroids. This is ascribed to the fact that dark bodies' phase function flattens with improving spatial resolution due to the reducing role of shadowing. A similar behaviour was observed on other dark asteroids, i.e., Ceres (Longobardo et al., 2019) and Bennu (Golish et al., 2021).

Finally, we focused the analysis on the artificial impact area by comparing phase curves before and after the impact. Currently, the only variations observed are within uncertainties, but we need to enlarge the dataset before to give any definitive conclusion.

**Acknowledgements.** We thank the ONC development/operations Team.

## References

Golish et al. (2021), *Icarus* 357, 113724

Longobardo et al. (2014), *Icarus* 240, 20-35

Longobardo et al. (2019), *Icarus* 320, 97-109

Longobardo et al. (2022), *A&A* 666, A185

Tatsumi et al. (2019), *A&A* 639, A83

# The shape distributions of sub-mm-sized impact experiment fragments from Allende meteorite

Tatsuhiko Michikami<sup>1</sup>, Akira Tsuchiyama<sup>2,3,4</sup>, Axel Hagermann<sup>5</sup>, and Sunao Hasegawa<sup>6</sup>

<sup>1</sup>*Faculty of Engineering, Kindai University, Hiroshima Campus, 1 Takaya Umenobe, Higashi-Hiroshima, Hiroshima 739-2116, Japan, (michikami@hiro.kindai.ac.jp),* <sup>2</sup>*Research Organization of Science and Technology, Ritsumeikan University, 1-1-1 Nojihigashi, Kusatsu, Shiga, 525-8577, Japan,* <sup>3</sup>*CAS Key Laboratory of Mineralogy and Metallogeny/Guangdong Provincial Key Laboratory of Mineral Physics and Materials, Guangzhou Institute of Geochemistry, Chinese Academy of Sciences (CAS), 511 Kehua Street, Wushan, Tianhe District, Guangzhou, 510640, China,* <sup>4</sup>*CAS Center for Excellence in Deep Earth Science, Guangzhou 510640, China,* <sup>5</sup>*Luleå University of Technology, Space Campus, 981 28 Kiruna, Sweden,* <sup>6</sup>*Institute of Space and Astronautical Science, Japan Aerospace Exploration Agency, Sagamihara, Kanagawa 252-8510, Japan.*

Several spacecraft have shown that kilometer-sized or smaller asteroids, such as Itokawa, Ryugu and Bennu, are covered with regolith particles. The shapes of regolith particles are considered clues to understanding their formation and evolution on asteroid surface. Ryugu particles are likely fragments resulting from impacts on the asteroid's surface. However, there has been a lack of laboratory impact experiments specifically examining the shapes of fragments in carbonaceous chondrites, which originate from carbonaceous asteroids like Ryugu and Bennu. In this study, we take the first step towards a better understanding of the shapes of impact fragments in carbonaceous chondrites. We conducted an impact experiment on the carbonaceous meteorite Allende and investigated the shape distributions of sub-mm-sized impact fragments using X-ray microtomography. As a result, we observed many fragments cross-sections along the chondrule boundary. In addition, these fragments tended to be rounder than previously observed impact fragment shapes. However, because the total number of these fragments is relatively small, the overall shape distribution of the fragments was found to be the same as that of previous impact fragment shapes. This finding will be useful for understanding the formation process of regolith layers on the asteroid surface, Itokawa particles, Ryugu particles, and Bennu particles scheduled to return to Earth.

# Spectral characterization of (98943) 2001 CC21, fly-by target of Hayabusa2#

Perna D.<sup>1</sup>, Barucci M.A.<sup>2</sup>, Belskaya I.<sup>2,3</sup>, Birlan M.<sup>4,5</sup>, Bourdelle de Micas J.<sup>1</sup>, Dotto E.<sup>1</sup>, Fornasier S.<sup>2</sup>, Hasegawa S.<sup>6</sup>, Ieva S.<sup>1</sup>, Inasaridze R.<sup>7</sup>, Ishiguro M.<sup>8</sup>, Kitazato K.<sup>9</sup>, Krugly Yu.<sup>3</sup>, Kuroda D.<sup>10</sup>, Mazzotta Epifani E.<sup>1</sup>, Palomba E.<sup>11</sup> and Yoshikawa M.<sup>4</sup>

<sup>1</sup>INAF – Rome Observatory, Italy. <sup>2</sup>LESIA – Observatoire de Paris, France. <sup>3</sup>Kharkiv National University, Ukraine. <sup>4</sup>IMCCE – Observatoire de Paris, France. <sup>5</sup>Astronomical Institute of the Romanian Academy, Romania. <sup>6</sup>ISAS-JAXA, Japan. <sup>7</sup>E. Kharadze Georgian National Astrophysical Observatory, Abastumani, Georgia. <sup>8</sup>Seoul National University, South Korea. <sup>9</sup>Aizu University, Japan. <sup>10</sup>Japan Spaceguard Association, Japan. <sup>11</sup>INAF-IAPS, Italy

To help solving uncertainties about the surface composition and possible heterogeneity of asteroid (98943) 2001 CC21, next fly-by target of Hayabusa2#, we acquired new visible and NIR photometric and spectroscopic data.

Visible (BVRI) spectrophotometry was obtained on November 2022 in the framework of the European NEOROCKS project, using the 1.2-m telescope located at the Haute-Provence observatory in France. Details of the observations and data reduction are given in [1]. The measured colors are within the range of values typical for S-complex. Figure 1 shows a comparison of the spectral behaviors of 2001 CC21 and templates of Sq, Sr, L and K-types according to the Bus-DeMeo classification scheme [2]. Our observations are well consistent with Sq or Sr types and do not support a L-type classification. This result is in agreement with recently published data on polarimetry and near-infrared spectrometry of this asteroid [3].

On January-February 2023, we also used the 2.6-m NOT telescope (La Palma, Canary Islands, Spain) to acquire visible spectra and NIR photometry of 2001 CC21 at different rotational phases. These data, currently under reduction, will allow us to further constrain its surface composition and possible heterogeneity.

On January 22, 2023 we observed 2001 CC21 in R band and covered the whole rotational period (Fig.2). The CCD observations were carried out using the 0.7-m telescope at the Abastumani Astrophysical Observatory, Georgia. The lightcurve amplitude is 0.75 mag and  $P_{rot} \sim 5.03$  hours.

Preliminary results confirm the S-complex taxonomy, and suggest a subtle spectral variation with the rotational phase. An overview of our results will be presented and discussed at the Symposium.

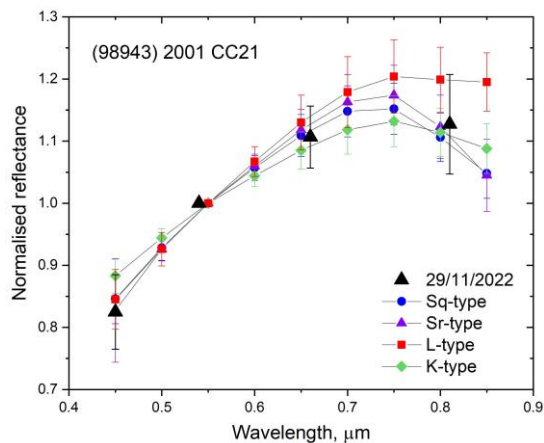


Figure 1. Comparison of 2001 CC21 obtained data with different asteroid taxonomic templates [4].

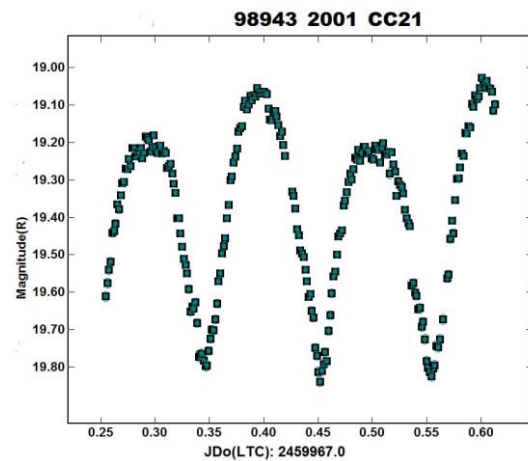


Figure 2. Lightcurve obtained on Jan 22, 2023.

## References

[1] Hromakina et al. 2021. MNRAS 520:3143. [2] DeMeo F. et al. 2009. Icarus 202:160. [3] Geem J. et al. 2023. MNRAS 525:L17. [4] Barucci et al. 2023. Abstract #2015, ACM 2023.

# Asteroid (142) Polana at 3 $\mu\text{m}$ and its Connection to Primitive Near-Earth Asteroids

Driss Takir<sup>1</sup>

<sup>1</sup>Jacobs, NASA JSC

**Introduction:** Impacts between asteroid-sized objects have dominated the solar system's history and played a significant role in forming asteroid families. The New Polana family is a low-inclination and the most prominent low-albedo family within the inner Main Belt between the  $\nu_6$  secular resonance at  $\sim 2.0$  AU and the 3:1 mean-motion resonance with Jupiter at  $\sim 2.5$  AU [1]. This family formed over 2000 Myr ago and is parented by the B-type asteroid (142) Polana [1]. [2] and [3] found that primitive near-Earth asteroids (NEAs), including Hayabusa2's asteroid target (162173) Ryugu and OSIRIS-REx's asteroid target (101955) Bennu, are likely disrupted fragments that originated during the formation of the New Polana family. Other possible sources of primitive NEAs in the inner Main Belt include the Clarissa, Erigone, Polana, and Sulamitis, families and the collisionally evolved background asteroids outside these families [2, 4].

The age of the solar system is longer than the collisional lifetime of asteroid Bennu [5], a rubble pile asteroid with a mean diameter of  $490.06 \pm 0.16$  m [6] and a spinning top-like shape [7]. Asteroid 142 Polana, the largest remnant of the New Polana family [1], has been spectrally ( $\sim 0.5$ - $2.5$   $\mu\text{m}$ ) and dynamically linked to asteroid Bennu [e.g., 2]. Bennu's spectra were measured over the wavelength range from 0.4 to 4.3  $\mu\text{m}$  with OSIRIS-REx Visible and InfraRed Spectrometer (OVIRS) [8]. Here, we investigate the compositional linkage of asteroids Polana and Bennu using 3- $\mu\text{m}$  Polana spectra measured at the Infrared Telescope Facility (IRTF).

**Results:** Polana's prism (0.7- 2.5  $\mu\text{m}$ ) spectra exhibit a broad concave feature centered  $\sim 1.21$   $\mu\text{m}$  with a band depth of  $\sim 11\%$ . The spectrum has a slight positive slope toward wavelengths greater than 1.2  $\mu\text{m}$ . We acquired two Prism sets of Polana, the first at 12:32 UTC and the second at 12:48 UTC on July 2<sup>nd</sup>, 2023. Spectra of the two prism sets are similar, showing no compositional heterogeneity in the observed surface of Polana. On the other hand, Polana's LXD (1.9– 4.2- $\mu\text{m}$ ) spectra do not reveal any pronounced spectral features in the  $\sim 2.0$ - $4.0$ - $\mu\text{m}$  spectral range, suggesting that this asteroid is not hydrated (Figure 1).

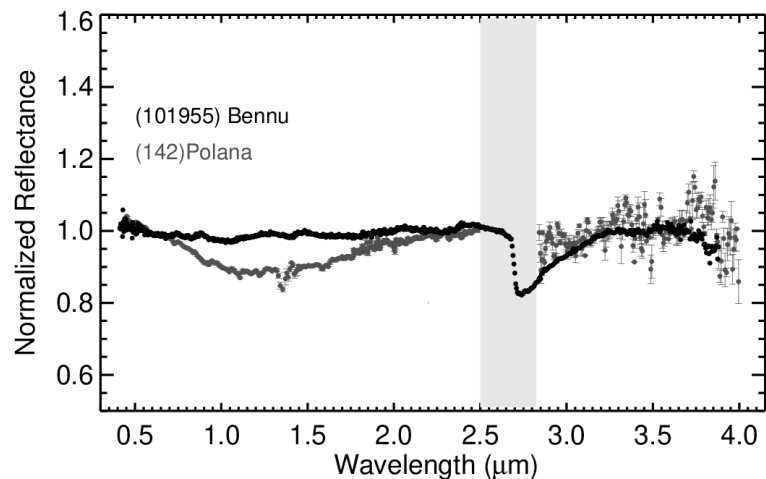


Figure 1. Spectra of asteroids Bennu and Polana. The  $\sim 1.2$ - $\mu\text{m}$  band in Polana is more pronounced than in Bennu. Bennu's spectrum is an average spectrum measured at the 10:00 a.m. station. Unlike Bennu, Polana does not show a pronounced feature at  $\sim 3$ - $\mu\text{m}$ . Slope-removed spectra are normalized at 2.2  $\mu\text{m}$ .

**Discussion:** Prism's spectrum of Polana shows a broad feature centered around 1.2  $\mu\text{m}$  (Figure 1), possibly due to amorphous iron-rich silicates abundant in least-processed CO carbonaceous chondrites that experienced minimal aqueous alteration and thermal metamorphism [10, 11]. Magnetite was also suggested to cause the 1.2- $\mu\text{m}$  feature in B-type asteroids [12]. The 1.2- $\mu\text{m}$  feature in the Polana spectrum is much deeper and more pronounced than Bennu's, suggesting that Polana has more abundant amorphous silicates or magnetite on its surface than Bennu. Polana was previously observed by [13], and its spectra SNR did not allow the authors to confirm the presence of a feature at  $\sim 3$ - $\mu\text{m}$ . In this work, the LXD spectrum of Polana was found to be featureless (does not exhibit a 3- $\mu\text{m}$  feature within two sigma), suggesting that Polana's surface is much less hydrated than Bennu's. Bennu's spectra were measured by OSIRIS-REx's OVIRS spectrometer, revealing that this primitive asteroid is hydrated (the 3- $\mu\text{m}$  band has a depth of  $\sim 20\%$ ) consistent with CM-, CI-, or CR-type carbonaceous chondrites [9]. In addition, Polana's LXD spectra do not indicate the presence of organics and/or carbonates, unlike Bennu, whose spectra were found to be consistent with carbonates dominated by calcite and aromatic and aliphatic organics with CH bonds [14, 15].

The lack of pronounced water (OH/H<sub>2</sub>O), organic materials, and carbonates features on asteroid Polana could be related to the degree of heating produced by shock metamorphism during the New Polana family-forming event and the ejecta reaccretion that contributed to additional heating. To lose most of its surface hydrated minerals, including serpentines, Polana had to be exposed to impact temperatures higher than  $\sim 800$  K [16]. Heating generated by disruptive collisions (families forming events) is substantial, where the temperature of almost all the parent bodies increases from 300 K (initial temperature) to 700 K [17]. [18] concluded that the hydration state of the members of a collisional family is heterogeneous and mainly depends on the impact energy level within the family.

Several factors can affect the degree of heating and shock metamorphism during family-forming events, including the impactor velocity and size, porosity within the asteroid's parent body, and material ejection efficiency. [19] found that in rubble-pile asteroids, the impactor velocity and size are the main factors responsible for high-grade shock metamorphism in impacts occurring in the Main Belt. According to these authors, changing the porosity, responsible for the overall energy

absorption within the parent body, from 10% to 30% in their simulations only slightly decreases the shock pressure and temperature.

Another possibility for explaining the discrepancy between Polana and Bennu in the 3- $\mu\text{m}$  band could be that the New Polana family-forming event exposed the parent body's deep interior. The dislodged Bennu fragment from the parent body contains phyllosilicates, organics, and carbonate, unlike the exposed interior of the parent body that does not include these materials.

Laboratory experiments on carbonaceous chondrites have shown that space weathering can also affect the spectral characteristics of these chondrites [20, 21]. For example, irradiating these carbonaceous chondrites can cause their near-infrared spectra to become bluer and brighter or redder and darker depending on several factors, including their initial albedo. Space weathering can also cause the band depth of mineral absorptions at 0.7 and 3.0  $\mu\text{m}$  to decrease respectively by 12 % to 50% [22]. Space weathering could cause the band depth at 3.0  $\mu\text{m}$  to degrade significantly over time. The New Polana is one of the older families in the Main Belt (~2000 Myr, [1]). Near-Earth asteroids' lifetimes are ~10 Myr [3]; therefore, Bennu would have been less exposed to space weathering than Polana was.

Exogenic materials and breccias are common in NEAs (e.g., [23]). Exogenous basaltic materials were discovered on the rubble pile asteroid Bennu, linked to inter-asteroid mixing that occurred at macroscopic scales after the end of the planetesimal formation [24]. It is possible that exogenic hydrated (in addition to basaltic) materials landed on Bennu, contributing to its hydration level.

Remote sensing observations of the primitive NEAs Ryugu and Bennu suggested that these two asteroids experienced different aqueous alteration histories, as revealed by the characterization of their surface composition using the 3- $\mu\text{m}$  band. The NIRS3 instrument on board Hayabusa2 detected a weak and narrow absorption feature centered around 2.27  $\mu\text{m}$  across the observed Ryugu's surface, attributed to hydroxyl-bearing minerals [25]. Returned samples from Ryugu confirmed that this asteroid has a similar composition to CI-type carbonaceous chondrites [26]. OSIRIS-REx's OVIRS detected a broader and deeper 3- $\mu\text{m}$  band in Bennu compared to NIRS3 observations of Ryugu. Based on their 3- $\mu\text{m}$  hydration features, it is more likely that Ryugu and Bennu came from different parent bodies with distinct aqueous alteration and thermal histories. With the current ground-based observations of Polana and due to strong Earth atmospheric absorptions that affect the ~2.7- $\mu\text{m}$  region, it is not feasible to fully assess if this asteroid has a 3- $\mu\text{m}$  band like the narrow and subtle band found in Ryugu. An approved JWST program to observe Polana (with the NIRSpec and MIRI instruments) will allow us to further investigate Polana's connection to Bennu and Ryugu.

**References:** [1] Walsh, K.J et al. 2013. *Icarus* 225, 283–297. [2] Campins, H. et al. 2010, *ApJ*, 721, L53. [3] Bottke, W. F et al. 2015, *Icarus*, 247, 191. [4] Arredondo, A. et al. 2021. Volume 368, 1. *Icarus*. [5] Bottke, W. F. 2015 et al. *Icarus* 247, 191–271. [6] Barnouin, O. S. et al. 2019. *Nat. Geosci.* 12, 247–252. [7] Lauretta, D. S. et al. 2019 *Nature* 568, 55–69. [8] Reuter, D. C. et al. 2018. *Space Sci. Rev.*, pp. 214, 54. [9] Hamilton, V. E et al. 2019, *Nat. Astron.*, 3, 332. [10] Cloutis, E.A. et al. 2012. *Icarus* 220, 466–486. [11] McAdam, M. and Gustafsson, A. 2021. *Icarus* 369 (2021) 114592. [12] Yang, B., Jewitt, D. 2010. *The Astronomical Journal*, 140:692–698. [13] Rivkin, A. S. et al. 2022 *Planet. Sci. J.* 3, 15. [14] Kaplan, H. H. et al. 2020, *Science*, 370, eabc3557. [15] Kaplan, H.H. et al. 2021. *A&A* 653, L1. [16] Nakamura, T. Yamato 2016. *Earth Planet. Sci. Lett.* 242, 26–38. [17] Davison, T.M et al. 2010. *Icarus* 208 468–481. [18] Michel, P. 2020. et al. *Nature Communications* volume 11, Article number: 2655. [19] Güldemeister et al. 2022. *The Planetary Science Journal*, 3:198 (12pp). [20] Lantz et al. 2018. Space weathering trends on carbonaceous asteroids: possible explanation for Bennu's blue slope? *Icarus* 302, 10–17. [21] Thompson, M. S. et al. *Icarus* 319, 499–511. [22] Matsuoka, M. et al. *ApJL* 890 L23. [23] Bischoff, A. et al. 2010. *Meteorit. Planet. Sci.* 45, 1638–1656. [24] DellaGiustina et al. *Nature Astronomy*, 5, January 2021 | 31–38. [25] Kitazato et al. 2019. Vol 364, Issue 6437 pp. 272–275. [26] Yada et al. 2021. *Nature Astronomy* volume 6, pages 214–220.

# Unveiling dark objects in Solar System: grain size effects on the infrared spectrum of mineral mixtures in presence of opaque components

G. Poggiali<sup>1,2</sup>, L. Fossi<sup>2</sup>, A. Wargnier<sup>1</sup>, J. Beccarelli<sup>3</sup>, J.B. Brucato<sup>2</sup>, M.A. Barucci<sup>1</sup>, P. Beck<sup>4</sup>, M. Matsuoka<sup>5</sup>, T. Nakamura<sup>6</sup>, M. Pajola<sup>3</sup>, S. Fornasier<sup>1,7</sup>, F. Merlin<sup>1</sup>, A. Doressoundiram<sup>1</sup>, T. Gautier<sup>8</sup> and G. David<sup>1</sup>

<sup>1</sup>LESIA-Observatoire de Paris, Université PSL, CNRS, Sorbonne Université, Université de Paris Cité, 92195 Meudon Principal Cedex, France (giovanni.poggiali@obspm.fr)

<sup>2</sup>INAF-Astrophysical Observatory of Arcetri, Firenze, Italy

<sup>3</sup>INAF-Astronomical Observatory of Padova, Padova, Italy

<sup>4</sup>Institut de Planétologie et d'Astrophysique de Grenoble, OSUG/CNRS, Grenoble, France

<sup>5</sup>The Geological Survey of Japan, National Institute of Advanced Industrial Science and Technology, Tsukuba, Japan

<sup>6</sup>Department of Geophysics, Tohoku University, Sendai Miyagi, Japan

<sup>7</sup>Institut Universitaire de France (IUF), 1 rue Descartes, F-75231 Paris Cedex 05, France,

<sup>8</sup>LATMOS, CNRS, Sorbonne Université, Université Versailles St-Quentin, Guyancourt, France

Dark surfaces characterize several bodies in the Solar System: from primitive carbonaceous asteroids to the enigmatic surface of Phobos and Deimos, our knowledge on the spectroscopic behaviour of low albedo surfaces is still incomplete. A dark surface can be related to multiple factors, for example presence of opaque material [1] or strong surface alteration [2]. In order to interpret remote sensing data, laboratory studies remain a pivotal tool to unveil the surface physical state and composition. Several processes can be simulated in the laboratory, but the preparation and analysis of complex mixing of analog material is one of the most fundamental tool and, at the same time, one of the most complex study when multiple components are used. In this work, we aim to study how dark material mixed with basaltic material at different grain sizes can affect the spectroscopic features from near- to mid-infrared (1.25-25  $\mu\text{m}$ ).

Our sample set includes four series of basaltic mix (feldspar and pyroxene), at different grain sizes from  $< 50 \mu\text{m}$  to  $1000 \mu\text{m}$ , mixed with amorphous carbon at increasing weight percentages from 1% to 50%. We analysed several features on the spectrum of each mineral mixture: (i) near infrared slope; (ii)  $2.7 \mu\text{m}$  OH-stretching band; (iii) Christiansen features; (iv) Reststrahlen band and Transparency feature. Measurements presented in this work [3], for the first time take into account a large wavelength range and point towards a critical effect of dark material with a different outcome for each grain size. Some of the most interesting results involved the slope and the different behaviour of the Reststrahlen band. This dataset will be a good support in the interpretation of upcoming data from Phobos Martian Moon eXploration mission, as well as in understanding of previous data from dark surfaces in the Solar System like Ryugu and Benu.

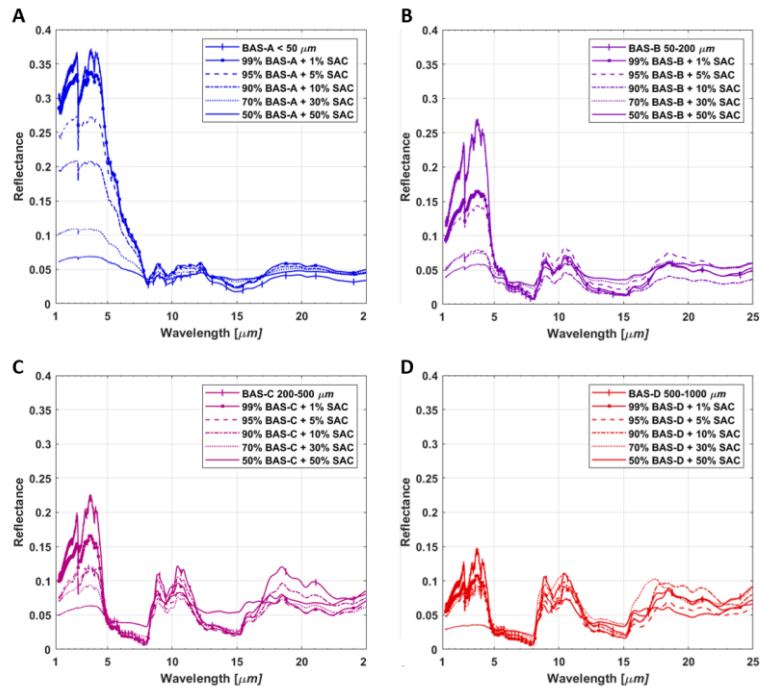


Figure 1. Infrared spectra of basaltic mixtures [BAS] at different grain sizes,  $< 50$ ,  $50-200$ ,  $200-500$  and  $500-1000 \mu\text{m}$ , with addition in different proportions, from 1 to 50%, with synthetic amorphous carbon [SAC].

## References

[1] Cloutis et al 1990, Icarus, 84 (2), 315-333 [2] Hasegawa et al 2022, The Astrophysical Journal Letters, 939, L9 [3] Poggiali et al 2023, Astronomy & Astrophysics (submitted)

# Investigating the effects of space weathering in Ryugu samples using coordinated microanalyses.

L. E. Melendez<sup>1</sup>, M. S. Thompson<sup>1</sup>, L. P. Keller<sup>2</sup>, S. A. Eckley<sup>3</sup>, and C. J. Snead<sup>2</sup>

<sup>1</sup>*Department of Earth, Atmospheric, and Planetary Sciences, Purdue University, West Lafayette, IN (melendl@purdue.edu)*

<sup>2</sup>*ARES, NASA Johnson Space Center, Houston, TX*

<sup>3</sup>*Jacobs, NASA Johnson Space Center, Houston, TX.*

**Introduction:** Airless planetary surfaces are characterized by a distinct lack of an atmosphere or magnetic field, leading to direct exposure to the effects of hypervelocity micrometeoroid impacts and solar wind ion irradiation [1]. These processes, cumulatively known as space weathering, gradually alter the microstructural and chemical properties of the grains on airless surfaces. Signatures of space weathering include vesiculated textures, amorphous grain rims (upper ~100 nm), solar flare tracks, and Fe-bearing nanoparticles (npFe) [2,3]. The accumulation of these microstructural space weathering characteristics, particularly the presence of npFe, alters the spectral properties of airless regoliths resulting in changes in spectral slope and reflectance of the surfaces, and the attenuation of characteristic absorption bands in the visible to near-infrared (Vis-NIR) wavelengths. These spectral changes complicate our ability to accurately interpret the mineralogy of airless bodies via remote sensing spectroscopy [1,4]. Studies of space weathering have primarily focused on anhydrous silicate minerals, reflecting the main components of the available returned samples from the Moon and S-type asteroid Itokawa [3,5,6]. However, our understanding of space weathering of primitive, organic-rich carbonaceous materials is still a work in progress. The Japan Aerospace Exploration Agency (JAXA)'s Hayabusa2 mission offered the first opportunity to directly investigate carbonaceous asteroids by returning samples from C-type asteroid (162173) Ryugu. Initial studies of Ryugu samples show mineralogical similarities to CI chondrites along with surface modifications consistent with space weathering. These surface modifications are primarily in the form of  $\mu\text{m}$ -thick silicate melts, amorphized phyllosilicates, glassy spherules, and burst vesicles [3,7]. Here, we report results from coordinated microanalytical techniques to further our understanding of the mineralogy and space weathering of carbonaceous materials.

**Samples and Methods:** We have been allocated two Ryugu particles returned by Hayabusa2; one particle collected at each of the two touchdown sites (A0152 and C0178). To understand the internal microstructure, mineralogy, and surface morphology of the two particles, we used X-ray computed tomography (XCT) to scan the samples using the Nikon XTH 320 micro-XCT at NASA Johnson Space Center (JSC) (Fig. 1). We also completed a higher-resolution sub-volume scan on the Zeiss Xradia 620 Versa at the University of Texas at Austin High Resolution X-ray CT Facility (UTCT) (Fig. 1). We segmented the dataset to identify different phases (e.g., sulfide minerals) and their spatial distribution using Dragonfly software. Due to the friable nature of the sample, small fragments were shed from the main mass during sample transport. We transferred <500  $\mu\text{m}$  fragments of each particle to SEM mounts covered with carbon tape and coated the fragments with evaporated carbon. The stubs were characterized using the Quanta 3D FEG focused ion beam scanning electron microscope (FIB-SEM) at NASA JSC using both backscatter (BSE) and secondary electron (SE) imaging detectors along with a 70  $\text{mm}^2$  SDD energy dispersive X-ray spectroscopy (EDS) detector (Fig. 2).

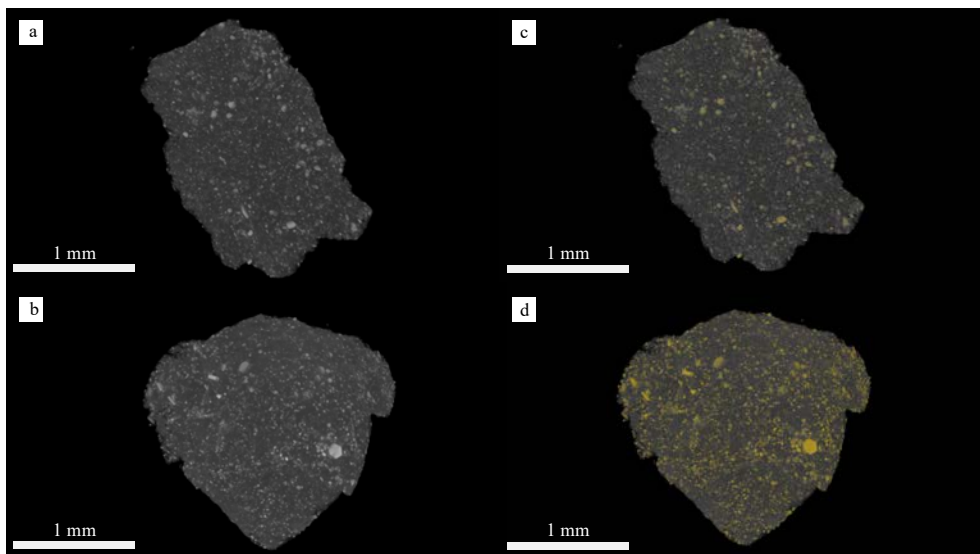


Figure 1. XCT scan of grain A0152 (a) and C0178 (b) with a resolution of 2.15  $\mu\text{m}$  per voxel. Volume renderings with bright (higher relative Z number) phases (i.e., pyrrhotite and magnetite) in yellow for A0152 (c) and C0178 (d).

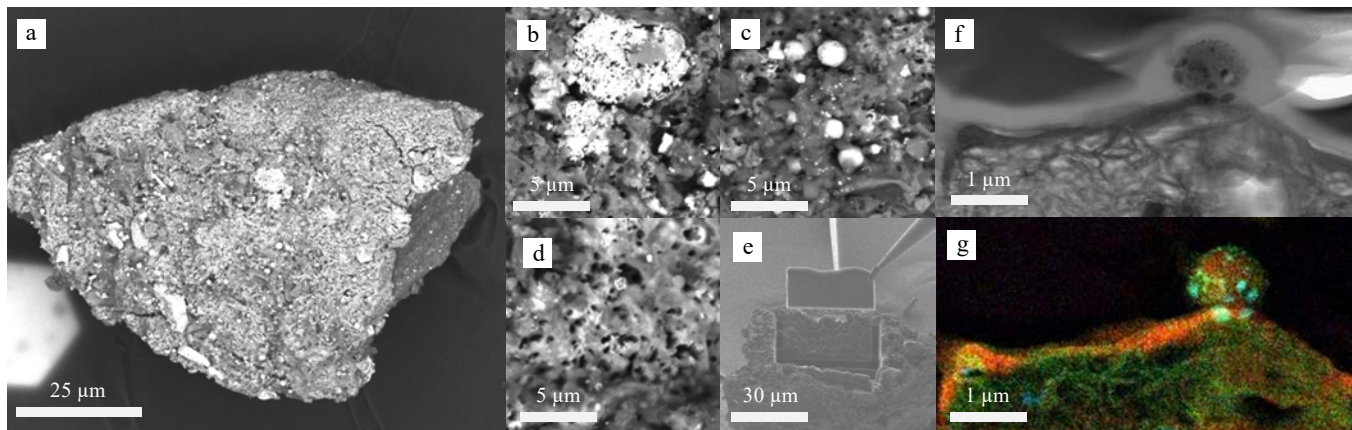


Figure 2. (a) Backscattered electron image (BEI) of one of the subparticles from A0152 with  $\text{Fe}_{1-x}\text{S}$  (e.g., pyrrhotite (b)) and characteristic signatures of space weathering, including (c) melt droplets and (d) vesicular textures. This melt deposit was targeted for further analysis in the TEM, with electron transparent thin sections prepared using FIB-SEM (e). The BF STEM image from the resulting FIB section (f) shows a region with a sub- $\mu\text{m}$  impact spherule on the surface on top of a darker melt layer. The composite RGB image (g) shows Mg (red), Fe (green), and S (blue), revealing a Mg-rich melt layer and a spherule with nanophase Fe and FeS inclusions.

Particles from chamber A that displayed vesicles or melt textures on their surface (indicators of micrometeoroid bombardment) were targeted for the preparation of three focused ion beam (FIB) sections for further analysis in the scanning transmission electron microscope (STEM). Particles from chamber C reflected the expected mineralogy of Ryugu but evidence of space weathering has not been identified on these grains. Two FIB sections were extracted from the phyllosilicate matrix and magnetite grains for comparison to the space-weathered regions of A0152. Bright field (BF) and dark field (DF) STEM images and chemical maps of the FIB sections were acquired using the JEOL 2500SE STEM equipped with a 60  $\text{mm}^2$  ultra-thin window silicon drift energy-dispersive EDS detector at JSC.

**Discussion and Conclusions:** XCT results indicate that the grain is a micro-breccia, and that hexagonal sulfide grains (likely pyrrhotite) are  $\sim 10$  to  $\sim 200$   $\mu\text{m}$  wide are distributed throughout the fine-grained phyllosilicate and carbonate-rich matrix. Magnetite ( $\text{Fe}_3\text{O}_4$ ) particles were also observed in both samples, exhibiting both framboidal and plaquette morphologies. 3D shape (SPO) and crystallographic (CPO) preferred orientations of sulfides (Fig. 1b) are being analyzed using Blob3D and 3DGrainMapper software, respectively. Currently, surface mesh renderings of A0152 and C0178 are being explored for evidence of impact cratering events, following [8]. SEM analysis of fragments from A0152 revealed vesiculated melt layers and frothy melt textures with melt spherules with embedded nanoparticles, resembling the deposits observed in simulated micrometeoroid bombardment [9]. STEM imaging confirmed the presence of Mg-rich phyllosilicates (serpentine and saponite), magnetite with variable morphologies, sulfides, and dolomite, consistent with previous studies of Ryugu samples indicating a low temperature aqueous alteration history [10, 11]. EDS analyses of these FIB sections of these regions revealed impact spherules and melt layers (up to 200 nm thick) containing abundant nanophase Fe-S and Fe-Ni-sulfides. Many of the nanoparticles are polyphasic, as opposed to the monomineralic nanoparticles observed in experimental samples. The melt layers have varying compositions depending on the underlying grain matrix: phyllosilicate grains have Ni-rich and Fe-poor melt layers while carbonate grains have Fe-, Mg- and O-rich melt layers. None of the particles analyzed thus far from C0178 exhibit textures characteristic of space weathering, which may be due to the comparatively ‘fresh’ nature of the subsurface sampling site, but we plan on proposing for additional grains for further analysis. We will continue to analyze these samples to better understand the effects of space weathering on carbonaceous regolith in preparation for the analysis of returned samples from asteroid Benu by OSIRIS-REx this year.

## References

- [1] Pieters C. M. and Noble S. K. (2016) *Journal of Geophysical Research* 121(10): 1865–1884.
- [2] Keller L. P. and McKay D. S. (1997) *Geochimica et Cosmochimica Acta* 61:2331–2341.
- [3] Noguchi T. et al. (2014) *Meteoritics & Planetary Science* 49:188–214.
- [4] Chapman C. R. (2004) *Annual Review of Earth and Planetary Sciences* 32:539–567.
- [5] Taylor L. A. et al. (2001) *Journal of Geophysical Research: Planets* 106:27985–27999.
- [6] Nakamura, T. et al. (2011) *Science* 333: 1113–1116.
- [7] Matsumoto, T. et al. (2021) *Hayabusa Symposium 2021*. NIPR.
- [8] Hamann, C. et al. (2023) *86<sup>th</sup> Annual Meeting of the Meteoritical Society Conference* Abstract 2692.
- [9] Thompson M.S. et al. (2019) *Icarus* 319: 499–511.
- [10] Matsumoto T. et al. (2021) *Nature Communications* 11:1–8.
- [11] Nakamura T. et al. (2022) *Science* 379: 6634–6785.
- [12] Tomioka et al. (2023) *Nature Astronomy* 7: 669–677.

## Impact-induced melting and fragmentation of C-type asteroid regolith inferred from impact craters on a large Ryugu sample

C. Hamann<sup>1</sup>, E. Bonato<sup>2</sup>, A. Maturilli<sup>2</sup>, K. Mahlow<sup>1</sup>, M. Patzschke<sup>3</sup>, R. Luther<sup>1</sup>, K. Kurosawa<sup>4</sup>, G. Alemanno<sup>2</sup>, S. Schwinger<sup>2</sup>, A. Van den Neucker<sup>2</sup>, M. Baqué<sup>2</sup>, L. Hecht<sup>1,5</sup>, A. Greshake<sup>1</sup>, and J. Helbert<sup>2</sup>

<sup>1</sup>Museum für Naturkunde Berlin, 10115 Berlin, Germany. <sup>2</sup>German Aerospace Centre, 12489 Berlin, Germany. <sup>3</sup>Bruker Nano Analytics, 12489 Berlin, Germany. <sup>4</sup>Planetary Exploration Research Center, Chiba Institute of Technology, Narashino 275-0016, Japan. <sup>5</sup>Institute of Geological Sciences, Freie Universität Berlin, 12249 Berlin, Germany.

The surfaces of airless planetary bodies are continually exposed to hypervelocity impacts of micrometeoroids and the influx of solar-wind ions as well as electromagnetic radiation emitted from the sun or other galactic sources [1,2]. Over time, these processes gradually alter the morphologies, microstructures, and chemical compositions of regolith grains exposed to space [3–7], which is collectively known as space weathering. Because space weathering alters the optical properties of space-exposed regolith (e.g., [2]), understanding space weathering of various types of planetary surfaces is critical for interpretation of remote-sensing data obtained from such surfaces and for matching various meteorite types to potential parent bodies. However, while the effects of space weathering on anhydrous regolith materials is well understood on the basis of samples returned from the Moon (e.g., [3,4]) and S-type asteroid Itokawa (e.g., [5–7]), space weathering of hydrous, carbonaceous-chondrite (C-type) like asteroidal surfaces is poorly understood so far. Samples returned by JAXA's Hayabusa2 mission from C-type near-Earth asteroid Ryugu (e.g., [8,9]) allow us to directly study the processes and products of space weathering of C-type asteroid regolith. Previous studies demonstrated that the uppermost surfaces of regolith grains returned from Ryugu's surface are amorphous and dehydrated due to influx of solar-wind ions [10,11]. In addition, small microcraters typically less than 10  $\mu\text{m}$  across and splashes of quenched melt—presumably impact melts—have been reported from several Ryugu samples [10,12]. To better understand the role of micrometeoroid impacts in space weathering of C-type asteroids, we studied the impact-crater population on Ryugu sample A0112, which is a large ( $3.0 \times 1.8 \text{ mm}$ ) regolith grain collected at the first touchdown site from the asteroid's immediate surface.

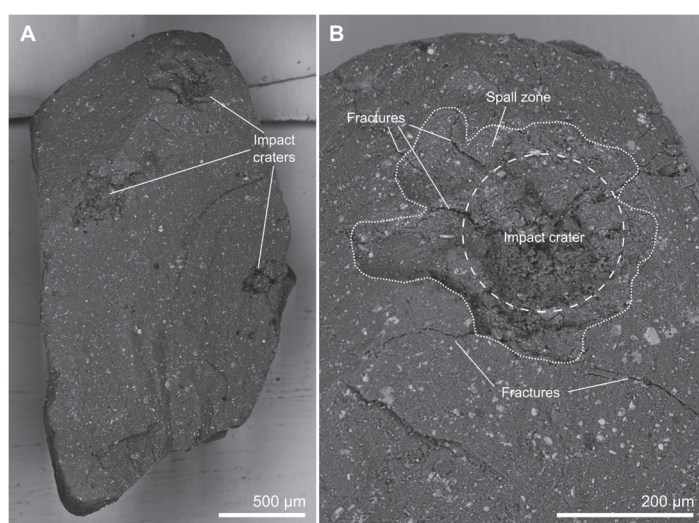


Figure 1. SEM-BSE images of the crater-covered side of A0112 (A) and the largest impact crater surrounded by a spall zone and surface-related, impact-produced fractures (B).

Scanning electron microscopy (SEM) at Museum für Naturkunde Berlin, Germany and Bruker Nano Analytics, Berlin, Germany as well as X-ray micro-computed tomography ( $\mu\text{CT}$ ) at Museum für Naturkunde Berlin revealed the presence of three large, crater-like depressions of 150–270  $\mu\text{m}$  diameter as well as of several smaller, circular pits of between 5 and 20  $\mu\text{m}$  diameter on one of the surfaces of A0112 (Fig. 1). High-magnification SEM imaging furthermore revealed the presence of frothy, highly vesicular materials that are interpreted as quenched impact melts (cf. [10]) lining the bottoms and walls of the large and many of the small crater-like depressions (Fig. 2). Reflectance spectra obtained at German Aerospace Centre, Berlin, Germany from the frothy material lining the largest crater-like depression are almost featureless between 2 and 4  $\mu\text{m}$  (Fig. 3) and resemble those obtained from the CI chondrite Ivuna heated to 700  $^{\circ}\text{C}$  [13]. Control

spectra obtained from the non-crater-bearing sides of A0112 are consistent with infrared spectra of other Ryugu samples (e.g., [14]) and showed pronounced spectral features at 2.71  $\mu\text{m}$  and 3.32 and 3.46  $\mu\text{m}$  that correspond to OH-bearing phyllosilicates and carbonates, respectively. Elemental analysis by energy dispersive X-ray spectroscopy (EDS) and EDS element distribution maps showed that the frothy materials are quenched silicate–sulfide emulsions, which suggests that the crater-like depressions and pits are impact craters. Quenched melt splashes up to 300  $\mu\text{m}$  across exist not only on the crater-bearing side of A0112, but also on an additional side of the sample. These are similar in chemical composition to the frothy layers described recently from other Ryugu samples [10] and invariably comprise silicate–sulfide emulsions. High-resolution EDS element distribution maps furthermore suggest that the quenched melts contain immiscible FeNi metal droplets (cf. [11]). In terms of major-element

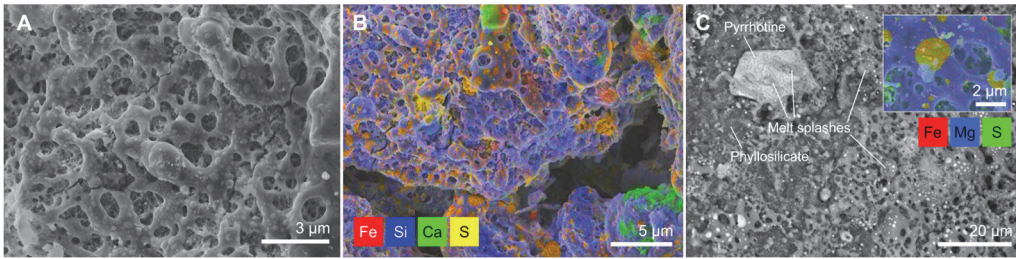


Figure 2. SEM-SE image (A) and element distribution map (B) of quenched impact melts lining the bottoms of the large impact craters on A0112. (C) SEM-BSE image of quenched melt splashes on the surface of A0112. A high-magnification element distribution map of the quenched melt splashes is shown in the inset.

subsurfaces adjacent to and below the large craters are intensely fractured; in particular, we observed fracture patterns resembling radial, concentric, and spallation fractures known from impact experiments in the strength regime (e.g., [17] and references therein). Consistent with lunar microcraters [17], large craters >150  $\mu\text{m}$  are surrounded by irregular spallation zones whereas small craters <40  $\mu\text{m}$  are almost perfectly bowl-shaped.

While investigations on the impact craters and quenched melts on A0112 are ongoing, our preliminary results provide information on the nature and magnitude of impact-induced processing of C-type asteroid surfaces in relation to solar wind-induced space weathering. Sample A0112 appears to be the most intensely shocked Ryugu sample investigated so far—the majority of smaller Ryugu samples were so far reported to be either essentially unshocked [18] or only marginally affected by micrometeoroid impacts, with solar wind-derived modifications dominating over impact-induced modifications [10–12]. Our findings of relatively large craters and abundant quenched impact melts on A0112 suggests that micrometeoroid impacts play an equally important role in space weathering of C-type asteroid regoliths as solar-wind induced modifications do. Impact-induced fracturing and spallation associated with the large craters on A0112 also informs on the efficiency of impact-induced fragmentation of grains in C-type asteroid regoliths [19]: Our observations suggest that spallation zones of micrometeoroid impact craters are likely sources of hydrated carbonaceous micrometeoroids arriving on Earth, contradictory to recent proposals based on unshocked to mildly shocked Ryugu grains [18]. This hypothesis is based on the fact that spall fragments ejected from spall zones surrounding hypervelocity impact craters are typically unshocked (e.g., [20]), but detailed numerical models using the iSALE shock physics code are currently being computed to probe peak pressures and temperatures in the spall zones surrounding the craters on A0112. If A0112's microcrater population is representative of Ryugu's surface, our results have relevance for evaluation of the relative roles of thermal [21,22] vs. impact-triggered [17] comminution of, and dust production from, C-type asteroid regolith.

Acknowledgments: We thank JAXA for allocation of Ryugu sample A0112.

## References

- [1] Hapke B. 2001. *Journal of Geophysical Research Planets* 106: 10039–10073. [2] Pieters C. M. and Noble S. K. 2016. *Journal of Geophysical Research Planets* 121: 1865–1884. [3] Keller L. P. and McKay D. S. 1997. *Geochimica et Cosmochimica Acta* 64: 2331–2341. [4] Pieters C. M. et al. 2000. *Meteoritics & Planetary Science* 35: 1101–1107. [5] Noguchi T. et al. 2011. *Science* 333: 1121–1125. [6] Noguchi T. et al. 2014. *Meteoritics & Planetary Science* 49: 188–218. [7] Thompson M. S. et al. 2014. *Earth, Planets and Space* 66: 89. [8] Yokoyama T. et al. 2023. *Science* 379: eabn7850. [9] Nakamura T. et al. 2023. *Science* 379: eabn8671. [10] Noguchi T. et al. 2023. *Nature Astronomy* 7: 170–181. [11] Melendez L. E. et al. 2023. Abstract #6286. 86<sup>th</sup> Meteoritical Society Meeting. [12] Nakato A. et al. 2023. *Earth, Planets and Space* 75: 45. [13] Hiroi T. and Pieters C. M. 1996. Abstract #551. 27<sup>th</sup> LPSC. [14] Pilorget C. et al. 2022. *Nature Astronomy* 6: 221–225. [15] Genge M. H. and Grady, M. M. 1999. *Meteoritics & Planetary Science* 34: 341–356. [16] Zolensky M. et al. 2022. *Meteoritics & Planetary Science* 57: 1902–1919. [17] Hörz F. et al. 2020 *Planetary and Space Science* 194: 105105. [18] Tomioka N. et al. 2023. *Nature Astronomy* 7: 669–677. [19] Flynn, G. J. 2009. *Planetary and Space Science* 57: 119–126. [20] Melosh H. J. 1984. *Icarus* 59: 234–260. [21] Delbo M. et al. 2014. *Nature* 508: 233–236. [22] Delbo M. et al. 2022 *Nature Geoscience* 15: 453–457.

chemistry, the melt splashes on A0112 match fusion crusts around the CI chondrites Orgueil and Alais [15] and resemble a quenched melt particle of likely impact-melt origin recently reported from Orgueil [16]. Furthermore,  $\mu\text{CT}$  scans revealed that the

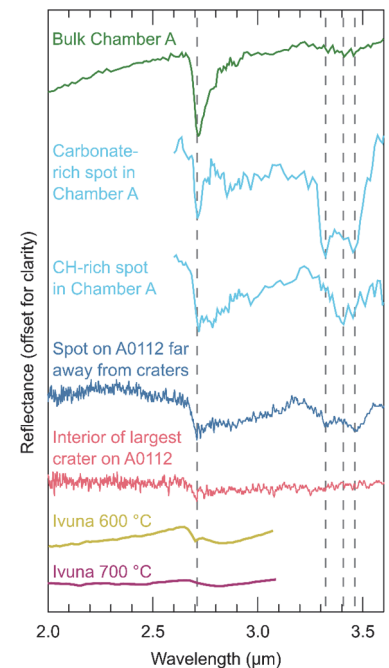


Figure 3. Reflectance spectra obtained from the largest impact crater on A0112 (red) compared against a spot far away from the craters (blue). Also shown are spectra of bulk A particles (green; [14]), carbonate- and CH-rich spots on Chamber A particles (light blue; [14]), and heated Ivuna CI chondrite (yellow and pink; [13]) for comparison.

# Temporal variability of thermal-cycling induced fracturing in chondrites

N. Latsia<sup>1</sup>, J. Borg<sup>1</sup>, E. Kaufmann<sup>1</sup>, M. Granvik<sup>1,2</sup> and A. Hagermann<sup>1</sup>

<sup>1</sup>*Luleå University of Technology*

<sup>2</sup>*University of Helsinki*

Regolith on asteroid surfaces was thought to be a result of micrometeoroid impacts [1], but some recent studies [2,3] claim that thermal fatigue is the dominant regolith production process on airless bodies. Thermal fatigue is produced by diurnal and/or annual variations on the surface temperature of asteroids and its efficiency depends on the heliocentric distance, the rotation period, and the thermal inertia of the asteroid's surface. A fundamental assumption of previous studies is that thermal fatigue remains effective over thousands, or even millions, of thermal cycles. However, the Kaiser effect, extensively studied in the field of fracture mechanics on terrestrial rocks, states that fracturing on materials ceases when previously exerted load levels are not exceeded [9]. Previous research has demonstrated that the thermal properties of CM2 chondrites depend on their mineralogy [11]. Thus, the thermal expansion coefficient of each mineral at specific temperature changes can be translated into different mechanical loads resulting from thermal fatigue.

We aim to observe the time-resolved crack propagation induced by thermal stresses over subsequent thermal load cycles in meteorites – acting as asteroid analogues – in order to understand the role of thermal fatigue in eroding asteroid surfaces. According to several studies, Ryugu is similar to CI [5,6,7,8] and CM [8] carbonaceous chondrites, and hence provides ground truth observations for these samples. We investigate CI, CM, and, for comparison, LL chondrites to examine the behaviour of thermal fatigue on different petrographic types of meteorites. The samples are subjected to a minimum of 100 cycles at  $\Delta T=210\text{K}$  as the temperature variation of C-type NEAs is 200K [2]. To identify the spatial occurrence of pre-existing and propagating cracks, the samples are scanned using X-ray tomography.

We aim to use non-destructive testing (NDT) methods to detect the time and frequency of crack initiation and propagation. NDT methods are used in many industries to identify and characterize the integrity of a material's surface and interior without interfering with its destruction [10]. The Kaiser effect predicts a decrease in the number of produced stresses as the number of thermal cycles increases, considering that the previous maximum and minimum temperatures of each cycle remain constant at  $170\text{C}^\circ$  and  $-40\text{C}^\circ$  respectively. If the Kaiser effect is applicable, we expect to see the effects of thermal fatigue wane after a few thermal cycles, suggesting that other mechanisms, such as chemical alteration, are contributing to the breakdown process of asteroids.

## References

[1] Housen K.R. et al. 1979. *Icarus* 39(3) 317-351. [2] Delbo M. et al. 2014. *Nature* 508(7495) 233-236. [3] Molaro J.L. et al. 2015. *JGR Planets* 120(2) 255-277. [4] Sakatani N. et al. 2021. *Nature Astron* 5(8) 766-774. [5] Yokoyama T. et al. 2022. *Science* 379(6634) abn7850. [6] Yada et al. 2022. *Nature Astron* 5(3) 214-220. [7] Kitazato K. et al. 2021. *Nature Astron* 5(3) 246-250. [8] Grott M. et al. 2020. *JGR* 125(12) e2020JE006519. [9] Kaiser J. 1950. A study of acoustic phenomena in tensile heat (PhD Thesis). [10] Dwivedi K. S. et al. 2017. *Materials Today* 5(2) 3690-3698. [11] Opeil C.P. et al. 2020. *MAPS* 55(8).

## **CALICO – an ESA M7 proposal to Explore Dwarf Planet Ceres**

Axel Hagermann<sup>1</sup>, Stefan Schröder<sup>1</sup> and the CALICO Consortium  
<sup>1</sup>*Luleå University of Technology*

Dwarf planet Ceres was the first member of the asteroid belt to be discovered. It is much richer in water than the other objects in the asteroid main belt, which suggests an origin elsewhere. Ceres' surface also shows clear signs of recent, possibly ongoing, geological activity and is regarded as the closest ocean world to Earth. The ocean worlds of the outer Solar System are of extreme interest for their potential to support biological activity over geological timescales. Unsurprisingly, the exploration of these enigmatic bodies is one of the priorities of ESA's Voyage 2050 strategy.

One region on Ceres of particular interest is Occator crater with its bright evaporite deposits, the so-called faculae. Formed by the extrusion of subsurface liquids, these deposits offer a window into Ceres' interior. In response to ESA's call for an M7 mission the international CALICO consortium, led by Luleå University of Technology, proposed CALICO (Ceres Autonomous Lander Into Crater Occator), a mission that will land in Occator crater and analyse the salt- and organics-rich deposits of Vinalia Faculae.

CALICO's science questions cover three themes:

1. Ceres as an active ocean world
2. Ceres' potential for habitability
3. Ceres' origin and evolution

CALICO will investigate carbon and organic material in the subsurface brine to assess the potential for complex organic chemistry, it will determine the physicochemical conditions to assess habitability. It will look for the chemical elements required for the building blocks of life and the elements required for biological energy production.

In order to unravel Ceres' origin and evolution, CALICO will pay special attention to the role of ammonia in its interior and the origin of Ceres' water as well as its magnetic history. CALICO will investigate the links between Ceres, asteroids, comets and carbonaceous chondrites.

In this talk, the mission concept and science payload of the CALICO mission will be presented, with a brief overview of the evolution and status of the proposal.

# Next Generation small body Sample Return mission: a concept study for a future Japanese mission to a comet

Hiroyuki Kurokawa<sup>1</sup>, Yuri Shimaki<sup>2</sup>, Naoya Sakatani<sup>2</sup>, Ryota Fukai<sup>2</sup>, Tatsuaki Okada<sup>2</sup>, Yoko Kebukawa<sup>3</sup>, Jun Aoki<sup>4</sup>, Atsushi Kumamoto<sup>5</sup>, Taichi Kawamura<sup>6</sup>, Satoshi Tanaka<sup>2</sup>, Eri Tatsumi<sup>2</sup>, Seitaro Urakawa<sup>7</sup>, Yuichi Tsuda<sup>2</sup>, Osamu Mori<sup>2</sup>, Takanao Saiki<sup>2</sup>, The Next Generation Small Body Sample Return WG

<sup>1</sup>University of Tokyo, <sup>2</sup>Japan Aerospace Exploration Agency, <sup>3</sup>Tokyo Institute of Technology, <sup>4</sup>Osaka University, <sup>5</sup>Tohoku University, <sup>6</sup>Université Paris Cité/Institut de Physique du Globe de Paris, CNRS, <sup>7</sup>Japan Spaceguard Association

The Next Generation small body Sample Return (NGSR) mission is a future solar-system exploration mission for sample return from a solar system small body under consideration. In February 2023, we newly launched the Science Working Group (WG) for the NGSR mission. The Science WG studies science goals and mission payloads of the NGSR. In collaboration with the Engineering WG, the Science WG aims to propose the NGSR as a strategic large-class mission which will be launched in 2030s by ISAS, JAXA. The strategic large-class mission will be selected in late 2024.

The NGSR targets a comet to bring back its subsurface materials and to explore its surface and internal structure. The Science WG defined the NGSR as a mission to unveil the origin of the solar system, namely, I) the origin of the solar-system “materials” in galactic evolution and II) the origin of the solar-system “bodies” to form planetesimals. For those science goals, we categorize science objectives as follows: Science objective I-1) unveiling the types of parent stars of the solar-system materials and their fractions, I-2) elucidating the origins of cometary organic matters, II-1) clarifying whether comets are rubble-pile or a pebble-pile bodies, and II-2) elucidating the formation environment of comets.

Science Goal I can be mainly achieved by sampling and analysis of subsurface materials of the target comet. In contrast to surficial materials that experienced alteration caused by space weathering and cometary activities, subsurface materials are thought to be pristine record of the original solar-system building blocks and, consequently, of the evolution of materials in our galaxy. Excavating and sampling subsurface materials are needed. Moreover, we are planning to install a mass spectrometer for in situ analysis of volatile materials that will potentially be altered and/or lost before the sample recovery.

Science Goal II can be mainly achieved by physical explorations of the interior structure with a radar and/or seismometer. Pebble-pile bodies (pristine first-generation of planetesimals) and rubble-pile bodies (disrupted and re-accreted planetesimals) should have different interior structures; only the latter are thought to possess meter-scale internal voids. The meter-scale heterogeneity can induce different propagation and reflection patterns for both radio and seismic waves.

# Intermediate bodies of Asteroids and the Moon from an Earth 3GMS model

Yasunori MIURA

*Department of Earth System Sciences, Faculty of Science, Yamaguchi University*

**Introduction:** Previous formation model of active water planet Earth has been static description of three material states (3MD) from various planetary and Earth sciences, which have been studied in details for more description as public definition from scientific researched fields to public library and museum for educated words. On the other hands, there are two unsolved items of 1) formation of active Earth planet, and 2) formation of inactive Asteroids and the Moon-Mars comparatively in the Earth-type planetary bodies. The main purpose of the paper is to new active Earth formation model called here as Active Three Material States (A3MS) to be continued to be young products on global and local sites of the planet now [1,2] (Table 1).

**Problem and characteristics of the previous 3MD model:** The previous 3MD model shows typical merits for the definition of each terminology word on educational sites of school, library, book and museum sites, though it shows some demerits for static description (without previous and future changes in details). This is mainly because planet Earth is not static but so active globally and locally as complicated phenomena to be changed one direction in wide Universe totally. In fact, we meet difficult spots (totally inactive with old history of primordial ages) to explain the details and comparison of extraterrestrial bodies of many Asteroids and the Moon and Mars even in neighbor celestial bodies in the Earth-type planetary bodies of the Solar System. We have to make more detailed figure of active planet Earth from various academic fields of geology, rocky minerals, mixed rocks, physics-chemistry-biology contently with news sciences of environmental and computer information. It is herewith keeping unsolved problem for many academic researched fields separated into individual academic fields [3,4].

**New model of present S3MS model:** It might be difficult to young scientists who study one of many academic fields precisely for present wide points of academic fields to be explained. However, new wider scientists (even older scientists) from fundamental Earth sciences (mineral-rock chemistry, micro-observation analyses and wide geological sciences) are possibly solved totally, where they should be studied also wide planetary fields of planet, physics-chemistry and active shock wave fields of quake-volcano-impacts (QVI) processes comparatively [5,6].

**Main points of new A3MS model:** The present A3MD model shows possible explanation for active process of rocky solid system of Earth which are activated energy naturally to change rocks from older to newer ages among three material states of solid, fluid liquid-to vapor air (SLV), which we can see younger trends of Earth totally. Compared short human life age, the solid of Earth are surely changed with longer times (due to life with light elements from carbon organic molecules with fluid system, compared with rocky system of Earth with longer ages of change comparatively with continued change processes).

**Meaning of existences of Atmosphere and Ocean systems on rocks (VLS) to Earth:** On primordial period of Earth, natural activation energy (QVI) has been started from no ocean system by gravitational quake (tidal) and rocky system to be found three planets and the Moon and Asteroids on the Earth-type planetary zone. However present earth site has change to produce, keep in side fluid and solid rock inside as mixture of fluids and vapors for some geological periods to be more active on dried primordial Earth with huge collisions (*i.e.* planetary-planetary, and/or multiple asteroids collision, where might be the most big chance of formation of global ocean mixed fluid system, where characteristic aspects of fluid liquid phases are showing boundary as image boundaries with irregular round shapes and light molecules with many elements involving between solid (rock) and vapor (air) phases formed as global ocean system on water planet Earth during decreased temperatures and continuous lower temperature among three material states (VLS) with new formed active phenomena of plate quake and volcano locally to keep moderate temperature kept in Earth system as moderate complex processes on active Earth now [2-4].

**Comparative differences of Earth and other celestial bodies:** The present A3MS model can be explained younger planet Earth

by natural active phenomena QVI events, which can be shown by major differences between young Earth and other bodies beyond Earth. The Mineral crystals defined from small to large sizes with colorful units of Earth can be formed by ocean plate activities of quake and volcano with interior magmatic melting with irregular but continuous movements under room-temperature condition of water-Earth, though inactive celestial bodies of Asteroids and the Moon show tiny assemblages of rocks with primordial ages. Continuous magma melting and metamorphic events are used to be formed final pure and large mineral crystal of quartz  $\text{SiO}_2$  and  $\text{CaCO}_3$  calcite carbonates (gem mineral) only water planet Earth. Ocean fluids are water mixed with many tiny elements from light to heavy metals brought by many asteroid impacts on ocean for longer geological periods, where as in similar process of mixed rocks to pure mineral crystal the mixed fluid of ocean water can be produces to pure water of rain and underground water or glacier ice globally as small percentage as pure products on active Earth. Life shows the similar A3MS assemblages on the rocks of water planet earth corporately as shown in different paper. This suggest comparatively organic life works can be seen in the complicated and continuous A3MS process discussed in this paper shortly, which it suggests that life system of organic compounds can be existed and continued the A3MS system on active Earth as we can observed clearly.

**Intermediate steps of various Asteroids 1M to the Moon 1M , and Mars 2MS from active planet Earth A3MS:** From whole differences between inactive 1MS (one material state) of Asteroids compared with 2MS (two material states) , the Asteroids show initial collision aggregates with various grains and rocks of Si-system (mountain rocks), Ca system (ocean rocks) and Fe-group system (heavy iron) with some contents of non-mineral elements of CO(HN)-systems synthesized in organic compounds on active planet Earth. From active A3MS model, products of non-mineral CHO-system are obtained in continuous and active planet Earth easily. For inactive Asteroids and the Moon, light element CHO-system groups are easily formed from products contained carbon elements (cf. steel parts) with impacted sample collections and/or analytical procedures by **collision less-shock** wave reactions by electron, ion and laser beam bombardments in analytical chambers are extremely carefully to be interpreted on the paper [5]. In short, many joined aggregates can be observed in many parts of the Asteroids before forming the Moon or Mars planet as intermediate solid-aggregated rocks before forming the water planet Earth with other active group of life-A3MS system groups [2].

Table.1 Comparison of material states MS of Earth, Asteroid and other extraterrestrial bodies.

Celestial bodies	Mineral or Rocks	Organic Life System
Earth (water planet)	Active three material states (A3MS) system	Non-mineral light elements (CHON) system
Asteroids, the Moon (Mars)	A material state (1MS) Intermediate mixture	Store in solid interior (mixture), Contamination?

**Summary:** The present work has been summarized as follows.

- (1) Active planet model A3MS can be explained on Earth, but others inactive bodies are 3MS on the Solar System.
- (2) This model can explain younger rock of Earth and older rocks of other bodies of Asteroids.
- (3) New large crystals and life system on Earth and mixed rocks on Asteroids might be explained in the model.
- (4) Aggregates observed in the Asteroids before forming the Moon or Mars planet as intermediate solid-aggregated rocks before forming the water planet Earth with other active groups of life system groups.

**References:** [1] Miura Y. (2018) IMA-22,1189. [2] Miura Y. (2023) JAMS. E5-15. [3] Wilson J.T. (1965) Nature, 207 (4995), 343-347. [4] Miura Y. (1996) Shock-Wave Handbook (SV, Tokyo),1073-1209. [5] Miura Y. and Kato T. (1993) AIP, 283, 488-492. [6] Miura Y. (1992) Celestial Mechanic. & Dynamical Astro. (KA), 54, 249-253.